This manuscript "The distribution of hydrogen/water in Al and Ti-containing forsterite: A thermodynamic model" is a preprint manuscript uploaded to EarthArvix which has not yet undergone peer review. It has been submitted for review. Subsequent versions may have different content.

The distribution of hydrogen/water in Al and Ti-containing forsterite: A thermodynamic model

Joshua M R Muir[*1], Michael Jollands[3], Feiwu Zhang[1], Andrew M. Walker[2]

Corresponding author: Joshua M R Muir j.m.r.muir@mail.gyig.ac.cn

1) Institute of Geochemistry, Chinese Academy of Sciences, 99 West Lincheng Road, Guiyang, Guizhou 550081, China
2) Department of Earth Sciences, University of Oxford, South Parks Road, Oxford OX1 3AN, United Kingdom
3) Lamont-Doherty Earth Observatory, 61 Rt 9W, Palisades, NY 10964, USA

Words:6637

Key Words: Forsterite; Water; Hydrogen; DFT; Point Defects; Titanium; Aluminium

Abstract

In forsterite the functional form of water is regard to be hydrogen. The distribution of this hydrogen across different sites in forsterite is important because it determines what rheological properties of forsterite are affected by water and how they are affected. In this study we use lattice dynamic Density Functional Theory (DFT) to build a thermodynamic model of hydrogen in forsterite that contains both Al and Ti sites. We find that Al does not cause significant variation in the distribution of water in forsterite but that Ti does. At low pressures we find that water favours either $(2H)_{Mg}^{X}$ or $\{Ti_{Mg}^{\cdot\cdot}(2H)_{Si}^{\prime\prime}\}$ with the latter favoured by low temperatures and high Ti contents. As pressure increases $(4H)_{Si}^{X}$ becomes the dominant site of water even in the presence of enstatite, high temperatures and high Ti contents. Thus two charge balance regimes are seen across normal experimental and upper mantle conditions. We predict the distribution of hydrous products along an upper mantle geotherm. The concentration of $(2H)_{Mg}^{X}$ likely controls Mg diffusion and conductivity and we find that this

peaks at ~100 km depth for 10 wt. ppm water, ~50 km for 100 wt. ppm water and at 0 km for 100 wt. ppm water before declining rapidly with depth beyond these points. The concentration of$(4H)_{Si}^{X}$ likely controls Si diffusion and the strength of forsterite. In relatively dry forsterite we find that there is initially a big increase in the concentration of $(4H)_{Si}^{X}$ with depth before a certain depth where the concentration of $(4H)_{Si}^{X}$ becomes insensitive to depth as it is the dominant product. As the crystal gets wetter the initial increase in concentration gets smaller and the depth at which $(4H)_{Si}^{X}$ becomes the dominant product becomes shallower. For 10 wt. ppm water $(4H)_{Si}^{X}$ concentration increases by 2 orders of magnitude over the first 200 km of a geotherm before obtaining a near consistent value whereas for 1000 wt. ppm water $(4H)_{Si}^{X}$ has a consistent concentration throughout the upper mantle. This suggests that nearly dry olivine gets considerably weaker as it descends into the mantle before a certain depth where it has consistent strength whereas wet olivine has a consistent strength throughout the upper mantle. We predict the water exponents of defect concentrations and find that they can vary strongly under different conditions particularly as charge balance regimes change. Water in forsterite thus behaves very differently in different P, T and water concentration regimes and extrapolation of mechanical properties between these regimes is extremely difficult.

Keywords: Forsterite; Hydrogen; Water; Titanium, Aluminium, DFT

1 Introduction

Water is a strong control on the properties of forsterite and olivine. Small amounts of water can lead to significant changes in strength ("hydrolytic weakening) (Demouchy et al., 2012, Girard et al., 2013a, Fei et al., 2013, Karato and Jung, 2003, Mei and Kohlstedt, 2000a, Mei and Kohlstedt, 2000b, Karato et al., 1986, Mackwell et al., 1985), texture development (Jung and Karato, 2001, Karato et al., 2008) and diffusion of cations and conductivity (Fei et al.,

2013, Fei et al., 2018). The upper mantle contains around 20-500 ppm water on average though it is likely most of it is quite dry <50 ppm with some regions considerably more enriched (Hirschmann, 2006, Demouchy and Bolfan-Casanova, 2016). Therefore we must understand the effect of water on olivine to understand the rheological properties of olivine in the upper mantle.

To determine the effect of water on mechanical properties we must know where it is located. Water that exists on Mg vacancies will have different effects on the properties of olivine that water that exists on Si vacancies for example. Water in forsterite is generally regarded as a series of hydrogen containing defects (see Equation 1) and thus the water sites in forsterite are all sites containing hydrogen and the distribution of water shall also be the distribution of hydrogen.

Experimentally there is a long literature examining the question of hydrous defects in olivine (Matveev et al., 2001, Le Losq et al., 2019, Berry et al., 2005, Tollan et al., 2018, Lemaire et al., 2004, Mosenfelder et al., 2006, Mosenfelder et al., 2011, Padron-Navarta et al., 2014, Berry et al., 2007a, Tollan et al., 2017, Blanchard et al., 2017) but in general 4 types of hydrated defects have been observed. These are (using Kroger-Vink notation): $(2H)^{X}_{Mg}$, $(4H)^{X}_{Si}$, $\{Ti^{\cdot\cdot}_{Mg}(2H)^{\prime\prime}_{Si}\}$ and $\{triv^{\cdot}_{Mg}(1H)^{\prime}_{Mg}\}$ where triv is a trivalent atom such as Fe(III) or Al (III) or Cr(III) (Tollan et al., 2017) most commonly Fe(III) (Blanchard et al., 2017). There is considerable disagreement about the relative favourability of these defects under different conditions. $(4H)^{X}_{Si}$ appears to be favoured at high pressures (Smyth et al., 2006, Xue et al., 2017, Withers and Hirschmann, 2008, Mosenfelder et al., 2006) but this may not be the case in the presence of Ti which forms (at low pressures) $\{Ti^{\cdot\cdot}_{Mg}(2H)^{\prime\prime}_{Si}\}$ with a water exponent of 1 (Tollan et al., 2017) or high temperatures which favour $(2H)^{X}_{Mg}$ (Walker et al., 2007). It is also important to know not just the most favoured defects but the concentrations of all hydrous

defects to precise levels as properties like diffusion can be affected by defects that are present even at ppt levels due to the low concentration of intrinsic defects (Muir et al., 2020).

Some theoretical work has been performed on the structure of hydrous defects in olivine. Early studies investigated the effect of hydrogen on defects using interatomic potentials (Wright and Catlow, 1994) but given how point defects alter the electronic structure of the crystal it has proven necessary to use electronic structure methods (Brodholt and Refson, 2000, Haiber et al., 1997, Braithwaite et al., 2002). More recent studies have investigated the interaction between hydrogen and trace elements such as titanium (Berry et al., 2007b, Walker et al., 2007) or boron (Ingrin et al., 2014) or attempted to link atomic scale models of the structure of various hydrous defects with the results of infra spectroscopy (Balan et al., 2011, Umemoto et al., 2011, Braithwaite et al., 2003). In general these studies have confirmed the structure of the various hydrous defects by determining the low energy forms but have not considered the effect of temperature or built a model of their energetic relationships to each other and to intrinsic defects with the exception of $(2H)^{X}_{Mg}$ and $(4H)^{X}_{Si}$ (Walker et al., 2007, Qin et al., 2018).

Thus in this work we shall use *ab-initio* calculations to build a thermodynamic model and probe the distribution of hydrogen in forsterite. We shall include Ti so as to examine the important $\{Ti^{\cdot\cdot}_{Mg}(2H)''_{Si}\}$ defect and Al to probe the effect of trivalent elements. These are two elements that occur in olivine to high concentrations (up to around 300 ppm) (De Hoog et al., 2010).

2 Methods

2.1 General Method

In this work we calculated the energy of different isolated defects in forsterite. This was done use lattice dynamics DFT. These energies are then used to calculate the energy of a series of reactions (see Results). We then determine the energy of different concentrations of these defects using the energies of these reactions and configurational entropy calculations and

115 determine the defect concentrations that give the minimum free energy at any particular
116 condition and this is the equilibrium distribution of defects.
117
118 *2.1 Defect calculations using density functional theory*
119 All calculations were performed with planewave DFT using version 16.11 of the CASTEP
120 code (Clark et al., 2005). On-the-fly ultra soft pseudopotentials were used with 2s, 3p and 3s,
121 2s and 2p, 3s and 3p, 1s and 3p, 3s, 4s and 3d electrons in the valence for Mg, O, Si, H and Ti
122 respectively. The PBE (Perdew et al., 1996) exchange correlation functional (a revised GGA
123 functional) was used alongside a planewave cutoff of 1000 eV and a (4x4x4) k-point grid in
124 reciprocal space (Monkhorst and Pack, 1976).
125 A (2x1x2) supercell of forsterite was used into which hydrous vacancies were inserted. After
126 placing defects in the supercell, the structure was then relaxed until the forces on all atoms
127 were less than 0.01 eV/Å and an energy tolerance of 1×10^{-5} eV/atom was repeated. Repeating
128 calculations with increased cutoffs changed the energy of the supercell by <0.1 meV/atom. A
129 (2x1x2) forsterite supercell was used to ensure that there was roughly 10 Å between repeating
130 vacancies in all directions, a distance we found to be sufficient to contain the important atomic
131 relaxations. For simulating $\{2Al_{Mg}^{\bullet}V_{Mg}''\}$ trios a (4x2x4) supercell was used due to the large
132 size of the defect. To approximate the dilute limit volumes were fixed to those of the pure
133 forsterite supercell for both static and QHA calculations. Defect energies were calculated at 0,
134 5, 10 and 15 GPa and at temperatures 1000, 1300, 1500, 1600 and 2000 K.
135 To calculate high temperature free energies the phonons of the most stable arrangements of
136 each type of defect were calculated using finite differences (displacements of 0.01 bohr) in the
137 CASTEP code (Clark et al., 2005). This was performed for at least 5 different volumes for
138 each system and the energy calculated as a function of volume with equations given in Muir et
139 al. (Submitted). The thermal expansion of forsterite was calculated and then at each

temperature and pressure the energy of each defect was calculated at the appropriate volume of forsterite at those conditions. More discussion on the approximations involved here is given in the supplementary information.

Our method for calculating non-hydrous vacancies is covered in Muir et al. (Submitted). 5 different hydrous defects were examined- $(2H)^{X}_{Mg}$, $(4H)^{X}_{Si}$, $(1H)'_{Mg}$, $H^{\bullet}_{Int}$ and $Ti^{\bullet\bullet}_{Mg}(2H)''_{Si}$. In each case their energy was sampled at each possible site in the crystal. $(2H)^{X}_{Mg}$ and $(1H)'_{Mg}$ were be placed at M1 and M2 sites in the crystal replacing a Mg atom. For $Ti^{\bullet\bullet}_{Mg}(2H)''_{Si}$ the Titanium was placed at an M1 or an M2 site replacing a Mg and the $(2H)''_{Si}$ was placed at an adjacent silicon site. The enthalpy of all possible arrangements of these two groups at adjacent sites was calculated (Table S3). For charged defects a correction was applied as outlined in Muir et al. (Submitted).

For $(2H)^{X}_{Mg}$, $(4H)^{X}_{Si}$, $Ti^{\bullet\bullet}_{Mg}(2H)''_{Si}$ and $(1H)'_{Mg}$ there are multiple possible arrangements of hydrogen in the vacancy. If we consider an arrangement of hydrogen as being each hydrogen bound to a specific oxygen (in an $(OH)^{-}$ group) we tested every possible arrangement of hydrogen with hydrogens pointing both into and out of the vacancy (Table S1-5). In each case the arrangement with the most stable enthalpy was used at high temperature.

2.2 Thermodynamic Minimisation

For any pressure and temperature, we first determined the energy of each defect at those conditions. This was done by projecting first along pressure and then along temperature using polynomials and points at 5, 10 and 15 GPa (uncorrected) and 1000, 1500 and 2000 K. The energy of each defect was then placed into the reactions found in the text and the energy of each reaction (E_i) determined at those conditions. We then used a series of minimisations to find the distribution of defects that gave the lowest free energy. In all cases the water content, Ti content and Al content were fixed for each minimisation.

Each combination of defects can be represented via a series of variables ($x_1 \ldots x_{22}$) where each variable represents one reaction in the text and goes from 0 (reaction does not proceed, all reactants) to 1 (all products).

The free energy of each distribution was determined with Equation 1:

$$\Delta G = \sum_i \Delta E_i \times x_i - TS_{confa} \quad \text{Equation 1}$$

with the first part related to forming the defects and the second part related to their configurational entropy. The first part is determined by simply the energy (E_i) of each reaction times by how far it progresses (x_i) while the second part is more complex. In short we determine for each defect the different enthalpies of its possible hydrogen arrangements, its placement on different lattice sites and its geometrical arrangements for defects that are pairs/trios and then we use the Gibbs entropy formula with the Stirling approximation to determine the configurational entropy of the whole system. Full details of our configurational entropy calculations and the approximations involved are given in the supplementary information. Using a bespoke solver (information in supplementary information) we vary each variable x1…x22, solving Equation 1 at each point, and do this until the energy no longer decreases and that is determined as the thermodynamic equilibrium distribution.

2.5 Pressure Correction

While DFT generally reliably reproduces pressure derivatives, the absolute pressures calculated by DFT are known to be systematically incorrect in that they are shifted in one direction. To correct for these we used a simple linear correction

$$P(V,T) = P^{DFT}(V,T) - P^{DFT}(V_0^{exp}) \quad \text{Equation 2}$$

Where the subscript 0 represents the value of a parameter at a reference volume. For this equation we used V_0^{exp} values of 287.4 Å^3 for olivine (Isaak et al., 1989), 74.71 Å for MgO (Speziale et al., 2001) and 832.918 Å^3 for enstatite (Kung et al., 2004). This provided

corrections of -4.95, -4.45 and -3.91 GPa respectively. The energy of our reactions were then adjusted to account for these different pressure corrections using our calculated dE/dP values. All pressures are presented corrected unless stated.

2.6 Units

In this work water concentrations are always given in wt. ppm H_2O, Ti concentrations in wt. ppm TiO_2 and Al in wt. ppm Al_2O_3.

3. Results

3.1 Water Reactions

Water could adsorb in forsterite via a reaction like:

$$Mg_{Mg}^{\times} + H_2O + \tfrac{1}{2}SiO_2 = (2H)_{Mg}^{\times} + \tfrac{1}{2}Mg_2SiO_4 \quad \text{Equation 3}$$

Determining the parameters of this reaction is difficult due to the presence of free water. Instead we can determine the favoured site for water in forsterite by calculating the energy differences between different sites. This was done for water defects, intrinsic defects and some selected non-hydrous extrinsic defects. A buffer reaction was used whose progress was set manually to control the SiO_2 activity. The following reactions were present in our model (using Kroger-Vink notation):

Hydrous Reactions

$$2(2H)_{Mg}^{X} + Si_{Si}^{X} + 3Mg_2SiO_4 \rightarrow (4H)_{Si}^{X} + 2Mg_{Mg}^{X} + 4MgSiO_3 \quad \text{R1}$$

$$(2H)_{Mg}^{X} + V_{Mg}'' \rightarrow 2(1H)_{Mg}' \quad \text{R2}$$

$$(2H)_{Mg}^{X} \rightarrow V_{Mg}'' + 2H_{Int}^{\cdot} \quad \text{R3}$$

$$(2H)_{Mg}^{X} + Ti_{Si}^{X} \rightarrow \left\{Ti_{Mg}^{\cdot\cdot}(2H)_{Si}''\right\} \quad \text{R4}$$

$3(2H)_{Mg}^{X} + Al_{Mg}^{\cdot} + Al_{Si}^{\prime} + Si_{Si}^{X} + 3Mg_2SiO_4 \rightarrow 2Mg_{Mg}^{X} + 2Al_{Mg}^{\cdot} + 2(3H)_{Si}^{\prime} + 4MgSiO_3$

R5

$(2H)_{Mg}^{X} + Si_{Si}^{X} + 2Mg_{Mg}^{X} + Al_{Mg}^{\cdot} + Al_{Si}^{\prime} + 4MgSiO_3 \rightarrow 2Al_{Mg}^{\cdot} + 2(1H)_{Mg}^{\prime} + Si_{Si}^{X} +$

$3Mg_2SiO_4$ R6

$(2H)_{Mg}^{X} + Si_{Si}^{X} + Al_{Mg}^{\cdot} + Al_{Si}^{\prime} + 3Mg_2SiO_4 \rightarrow 2Al_{Si}^{\prime} + 2H_{Int}^{\cdot} + 2Mg_{Mg}^{X} + 4MgSiO_3$ R7

<u>Anhydrous Extrinsic Reactions</u>

$Al_{Mg}^{\bullet} + Al_{Si}^{\prime} + 2Mg_{Mg}^{X} + 4MgSiO_3 \rightarrow 2Al_{Mg}^{\bullet} + V_{Mg}^{\prime\prime} + Si_{Si}^{X} + 3Mg_2SiO_4$ R8

$2Al_{Mg}^{\bullet} + V_{Mg}^{\prime\prime} \rightarrow \{2Al_{Mg}^{\bullet}V_{Mg}^{\prime\prime}\}$ R9

$Al_{Mg}^{\cdot} + Al_{Si}^{\prime} \rightarrow \{Al_{Mg}^{\cdot}Al_{Si}^{\prime}\}$ R10

<u>Anhydrous Intrinsic Reactions</u>

$Mg_{Mg}^{X} \rightarrow V_{Mg}^{\prime\prime} + Mg_I^{\bullet\bullet}$ R11

$O_O^{X} \rightarrow V_O^{\bullet\bullet} + O_I^{\prime\prime}$ R12

$Si_{Si}^{X} \rightarrow V_{Si}^{\prime\prime\prime\prime} + Si_I^{\bullet\bullet\bullet\bullet}$ R13

$2V_{Mg}^{\prime\prime} + Si_{Si}^{X} + 3Mg_2SiO_4 \rightarrow V_{Si}^{\prime\prime\prime\prime} + 2Mg_{Mg}^{X} + 4MgSiO_3$ R14

$Mg_{Mg}^{X} + O_O^{X} + MgSiO_3 \rightarrow V_{Mg}^{\prime\prime} + V_O^{\bullet\bullet} + Mg_2SiO_4$ R15

$Mg_2SiO_4 \rightarrow Mg_I^{\bullet\bullet} + O_I^{\prime\prime} + MgSiO_3$ R16

$Si_{Si}^{X} + 2O_O^{X} + Mg_2SiO_4 \rightarrow V_{Si}^{\prime\prime\prime\prime} + 2V_O^{\bullet\bullet} + 2MgSiO_3$ R17

$Si_{Si}^{X} + 2Mg_{Mg}^{X} + 4MgSiO_3 \rightarrow 2V_{Mg}^{\prime\prime} + Si_I^{\bullet\bullet\bullet\bullet} + Si_{Si}^{X} + 3Mg_2SiO_4$ R18

$Mg_2SiO_4 \rightarrow Mg_I^{\bullet\bullet} + O_I^{\prime\prime} + MgSiO_3$ R19

$Si_{Si}^{X} + 3Mg_2SiO_4 \rightarrow V_{Si}^{\prime\prime\prime\prime} + 2Mg_I^{\bullet\bullet} + 4MgSiO_3$ R20

$2Mg_{Mg}^{X} + Si_{Si}^{X} + 4O_O^{X} \rightarrow 2V_{Mg}^{\prime\prime} + V_{Si}^{\prime\prime\prime\prime} + 4V_O^{\bullet\bullet}$ R21

<u>Buffer Reaction</u>

R22) $MgSi_2O_4 \rightarrow MgO + MgSiO_3$ R22

Energies of these reactions are presented in Table 1 and Table S6. Despite using Kroger-Vink notation we allow the number of sites in forsterite to vary if forsterite is created or destroyed (such as in R23 and R24) as explained in Muir et al. (2020) but this has no noticeable effect on the results. Defects in {} brackets are charge pairs that are associated with each other, this is represented in our model by placing them on adjacent sites. For most charge pairs the energy gain from randomly placing them in the crystal is larger than the energy gain (due to electrostatics) from pairing them. This is explored in Table S7. There are three exceptions. $\{Ti_{Mg}^{\cdot\cdot}(2H)_{Si}''\}$ pairs have large binding energies (5-6 eV) and thus should always occur as pairs and are represented as such in our model (R4). $\{Al_{Mg}^{\cdot}Al_{Si}'\}$ pairs and $\{2Al_{Mg}^{\bullet}V_{Mg}''\}$triplets have middling binding energies and could occur as bound pairs/triplets in some situations. We allow for these systems to be both bound and unbound through reactions R9 and R10. We find that R9 does not happen in any of our explored conditions (as speculated in (Muir et al., 2020)) and all $\{2Al_{Mg}^{\bullet}V_{Mg}''\}$ triplets are unbound. We find that R10 happens moderately with $\{Al_{Mg}^{\cdot}Al_{Si}'\}$ bound pairs being anywhere from 1.01% to 99.81% of the $Al_{Mg}^{\cdot}Al_{Si}'$ pairs with the remaining percentage being unbound. Lower temperatures, higher Al concentrations and pressures lead to more bound $\{Al_{Mg}^{\cdot}Al_{Si}'\}$ pairs with water concentration having little effect. All reactions above have been written in a system where $MgSiO_3$ is present and numbers shall be presented as such. This can be converted to a system where MgO is present by using R22 in appropriate amounts. Al is placed intitally as an unbound pair of $Al_{Mg}^{\cdot}$ and Al_{Si}'. Ti is initially placed as a 4+ cation replacing Si (Berry et al., 2007b).

In this formulation water starts (arbitrarily) as $(2H)_{Mg}^{X}$ and then reacts until it reaches its thermodynamically favoured distribution across the various water sites. The possible sites for water are $(2H)_{Mg}^{X}$ (concentration of these sites shall be referenced as [HMg]), $(4H)_{Si}^{X}$ ([HSi]), $\{Ti_{Mg}^{\cdot\cdot}(2H)_{Si}''\}$ ([TiH]), $(1H)_{Mg}'$([1HMg]), $H_{int}^{\cdot}$ ([HFree]) and $(3H)_{Si}'$ ([3HSi]).

257

258 *3.2 Pure Forsterite*

259 We predict water in pure forsterite to produce 2 defects $(2H)^{X}_{Mg}$ and $(4H)^{X}_{Si}$. Two other
260 defects have been proposed in the literature and these are $(1H)'_{Mg}$ and $H^{\bullet}_{Int}$ produced by R2
261 and R3. While there is evidence that $(1H)'_{Mg}$ is produced in the presence of ferric iron (Berry
262 et al., 2007a, Blanchard et al., 2017) there is no clear evidence for the production of $(1H)'_{Mg}$
263 and $H^{\bullet}_{Int}$ in forsterite. We find these to be extremely minor products. In none of our runs did
264 the concentration of $(1H)'_{Mg}$ exceed 1x10^{-20} (the limit of detectability we set in our model) and
265 $H^{\bullet}_{Int}$ never exceeded 1x10^{-7} defects/f.u. and 1 x10^{-9} defects/f.u. in the absence of Al (Figure 1).

266 To confirm this we looked at R2 and R3 as isolated reactions occurring by themselves with no
267 other reactions to consider. R2 proceeding to the right is disfavoured by enthalpy and produces
268 no entropy gain and thus $(1H)'_{Mg}$ is never favoured to be produced over $(2H)^{X}_{Mg}$. R3
269 proceeding to the right is strongly disfavoured by enthalpy and strongly favoured by entropy
270 and thus occurs at small water contents. At 0 GPa (corrected) and 2000 K we find that $H^{\bullet}_{Int}$
271 exceeds $(2H)^{X}_{Mg}$ only when water content is <0.2 wt. ppb. This is an extremely small water
272 content. Lower temperatures or higher pressures will decrease the concentration at which $H^{\bullet}_{Int}$
273 is favoured and the amount of $H^{\bullet}_{Int}$ that is formed (see Table 2). Thus $H^{\bullet}_{Int}$ and $(1H)'_{Mg}$ are
274 not substantially stable products in these systems and shall be ignored in the rest of this work.
275 In Kohlstedt (2006) exponents of water concentrations are derived based upon charge balance
276 conditions and we find that for any reasonable amount of water (above 1 ppb) the charge
277 balance condition is $[p^{\bullet}] = 2[H'_{Me}]$ under this scheme.

278 In pure forsterite either $(2H)^{X}_{Mg}$ or $(4H)^{X}_{Si}$ can be the dominant water product (Figure 1). High
279 temperature encourages the formation of $(2H)^{X}_{Mg}$ (Figure 2) as it increases the configurational

entropy (by having 2 defect sites to 1 for $(4H)_{Si}^{X}$), high water concentration stabilises $(4H)_{Si}^{X}$ (Figure 1, again due to entropy) and high pressure (Figure 3) encourages the formation of $(4H)_{Si}^{X}$ as seen previously experimentally (Smyth et al., 2006, Xue et al., 2017, Withers and Hirschmann, 2008, Mosenfelder et al., 2006). This is because R1 which produces $(4H)_{Si}^{X}$ eliminates a vacancy which are large and disfavoured by pressure. We plot the pressure at which this occurs in Figure 4. Decreasing SiO_2 activity (by swapping enstatite for MgO) increases $(2H)_{Mg}^{X}$ stability considerably but the mantle is more closely represented by an enstatite buffer so from now on all of our results will be buffered by enstatite as presented in the reactions above. For large amounts of water (>~520 wt. ppm) $(4H)_{Si}^{X}$ is always the dominant water product even at 2000 K and 0 GPa. In upper mantle conditions with low amounts of water <500 wt. ppm water should switch from $(2H)_{Mg}^{X}$ to $(4H)_{Si}^{X}$ at some characteristic depth depending upon water content and temperature as shown in Figure 4.

A key variable in predicting water effects is the water exponent (r) generally defined as:

$$[Defect] \propto f_{H_2O}^{r} \quad \text{Equation 4}$$

In simple systems where each product can be described by a single equation (such as $(4H)_{Si}^{X}$ being solely produced by R1) and where configuration entropy is unimportant each product can be described by a single number which should be relatively insensitive to pressure, temperature and water concentration. In complex systems r will vary significantly with condition. We examine this in our system in Table 3.

In our system we do not have water fugacity but we can instead determine

$$[Defect] \propto [H_2O]_{bulk}^{r} \quad \text{Equation 5}$$

All values of r in this study shall refer to that of Equation 5 rather than 4. While Equation 4 and 5 have occasionally been treated as the same in previous literature they are not as Equation

4 has additional mixing terms that are not present in Equation 5. For Equation 5 the dominant water defect (the species that provides the charge balance regime) in forsterite should have an r that trends towards 1 while the exponents of the other water species are (in a simple system) dependent on how the minor water species relate to the major species. For example in a simple system where $(2H)^X_{Mg}$ is the major product it will have an exponent of 1 and $(4H)^X_{Si}$ will have an exponent of 2 based on R1. Conversely where $(4H)^X_{Si}$ is the major product it will have an exponent of 1 and $(2H)^X_{Mg}$ will have an exponent of 0.5 in a simple system. This can be seen in Table 3 for the Ti and Al containing system where at 2000 K and 0 GPa the exponent for $(2H)^X_{Mg}$ is 1 and $(4H)^X_{Si}$ is 2 (a system charge balanced by $(2H)^X_{Mg}$) but at 10 GPa these values are 0.5 and 1 (a system charge balanced by $(4H)^X_{Si}$). The exponents for $(2H)^X_{Mg}$ and $(4H)^X_{Si}$ as well as those of V''_{Mg} and V''''_{Si} always have a roughly 1:2 ratio because the Si vacancies are controlled by R1 and R14 respectively.

Our exponents were determined by fitting to:

$$ln[Defect] = a + rln[H_2O]_r \quad \text{Equation 6}$$

where a is a variable and the results are presented in Table 3. We find that exponent values are quite variable and often do not have their ideal value. At low temperatures and high pressures, the exponents approach their ideal values but as temperature rises or pressure decreases the exponents are always above their ideal values due to configurational entropy which relatively increases in both of these cases. Exponents were measured in Tollans *et al.* 2017 where they found values of 2.5 for $(4H)^X_{Si}$, 1.1 for $(2H)^X_{Mg}$ and 0.9 for $\{Ti^{\cdot\cdot}_{Mg}(2H)''_{Si}\}$ using Equation 4 instead of 5. These values are all slightly higher than the ideal values with deviations coming both from possible non-ideality of their NaCal fluid but also the presence of some configurational entropy will always raise exponents above their ideal values as shown here. Thus the water exponents r in real systems should be heavily dependent upon pressure,

temperature and chemical environment and can vary across common water ranges with particularly large variations as the major hydrous product changes (Figure 1).

The presence of water will also have a large effect on the intrinsic defects of forsterite as shown in Figure 5. In general the presence of water suppresses the formation of intrinsic defects. This is because they form due to configurational entropy gains upon formation and these gains are relatively decreased in the presence of water (or other extrinsic defects).

Each atom in Mg_2SiO_4 can have a vacancy or an interstitial defect. Mg vacancies (V''_{Mg}) and Mg interstials ($Mg_I^{\bullet\bullet}$) are the most prominent extrinsic defects due to the favourability of R11 over other extrinsic reactions (Table 1 and S6). $V_O^{\bullet\bullet}$ is the next most prominent vacacy due to R15 and then V_{Si}'''' due to R14. We find that V_{Si}'''' is produced by R14 and not by any of the other V_{Si}'''' reactions which are higher in energy (Table S6). Thus the concentration of V_{Si}'''' is proportional to the concentration of V''_{Mg} which is a reactant in R14. Previous thermodynamic models have used R13 as a base for V_{Si}'''' (Stocker and Smyth, 1978) and thus came to different conclusions about the effect of various conditions on V_{Si}'''' but we find this to be extremely unfavourable. No mechanism that we tested that produces O_I'' or $Si_I^{\bullet\bullet\bullet\bullet}$ was favourable and thus the production of these defects was below the detection limit ($1x10^{-20}$ defects/f.u.) and likely far below this limit based on the extremely high energies of all reactions that produce these interstitials. Thus we conclude Si and O interstitials are not present in forsterite to any significant degree.

The effect of water on intrinsic defect exponents has been previously speculated in (Kohlstedt, 2006). Using speculations on the key defect producing reactions and the effect of water on K they postulated that water has no effect on Si and Mg vacancies (r=0) in the charge balance regime $[p^{\bullet}] = 2[H'_{Me}]$. This was extended to O vacancies (Fei et al., 2016) which also had r=0. We find, however (Table 3) that generally these products have negative exponents due to the

suppressive effect of water on their configurational formation entropy. The exponent of V''_{Mg} is sometimes positive due to the effects of R3 which creates V''_{Mg}. While R3 only operates in very small amounts relative to other water products it can still create V''_{Mg} at significantly greater rates than are produced intrinsically. We cannot determine exponents for V''''_{Si} directly because the concentration of V''''_{Si} is extremely low and often below our detection limit but as the concentratioin of V''''_{Si} is controlled entirely by R14 this exponent should be close to twice that of V''_{Mg}.

We find significant deviations from the r values of literature (r=0) particularly in the presence of Al and Ti. This is unsurprising as configurational entropy (which deviates from these perfect values) will always be important for intrinsic defects as it is fundamental to their creation. All the intrinsic defect forming reactions have high positive enthalpies meaning that they only proceed forwards due to the configurational entropy gain of producing defects. Thus in most scenarios the exponents for intrinsic defects will be heavily sensitive to configurational entropy and deviate from their normal values. This means that when dealing with intrinsic defects their exponents are particularly hard to extrapolate across temperature and pressure space and must be measured at the desired conditions.

The Effect of Al

As shown in Figure 1 Al has no large effects on the distribution of water in forsterite. Some $(3H)'_{Si}$ is produced through R5 and a very small amount of $H_{Int}^{\cdot}$ through R7 though considerably more than produced in pure forsterite. R6 is not significant and never produces any detectible amounts of $(1H)'_{Mg}$. R8 can produce large amounts of V''_{Mg} leading to an increase of the concentration of V''_{Mg} compared to pure forsterite but this effect is suppressed by water and is neglible beyond ~5 wt. ppm water (Figure 5). The effects of this reaction are explored in more detail in Muir et al. (2020). R5, R7 and R8 all increase the ratio of $Al^{\bullet}_{Mg}/Al'_{Si}$

from its initial value of 1 with this effect mostly controlled by R5. This ratio is plotted against water concentration in Table S8. We find that these changes are generally small with $Al^{\bullet}_{Mg}$ usually being <0.1% larger than Al'_{Si} but at high temperatures, low pressures, low Al content and high water content the $Al^{\bullet}_{Mg}/Al'_{Si}$ ratio can become significant and a strong measure of water content in forsterite.

The Effect of Ti

Ti has a large effect on water distribution through the formation of $\{Ti^{\cdot\cdot}_{Mg}(2H)''_{Si}\}$ as R4 is very favourable. As shown in Figure 1 and 3 at low pressures $\{Ti^{\cdot\cdot}_{Mg}(2H)''_{Si}\}$ can compete with $(2H)^{X}_{Mg}$ to be the major product. Low temperatures (Figure 2) and high Ti concentrations (Figure 6) favour $\{Ti^{\cdot\cdot}_{Mg}(2H)''_{Si}\}$ over $(2H)^{X}_{Mg}$ while pressure (Figure 3) and water concentration have little effect (Figure 1). R4 is insensitive to pressure (Table 1) and thus with increasing pressure $\{Ti^{\cdot\cdot}_{Mg}(2H)''_{Si}\}$ is disfavoured against $(4H)^{X}_{Si}$ similar to $(2H)^{X}_{Mg}$. This is seen in Figure 4 where Ti makes only small changes to the pressure at which $(4H)^{X}_{Si}$ is dominant.

Similar to Al the site of Ti is a measure of water content. As shown in Table S9 the $Ti^{X}_{Si}/Ti^{\cdot\cdot}_{Mg}$ ratio is roughly linear with water content for a fixed P, T and Ti concentration. The ratio varies strongly and nonlinearly with P and T so fitting a universal law is complex and will have overlapping points but inside a known P and T the water content can be solved. This provides both a test of unknown water content if this ratio can be measured and a test of our model if water content is known.

4. Discussion

The distribution of water in the upper mantle

Figure S4 shows the distribution of water along an upper mantle geotherm (Ono, 2008) (Table S10) in a pure forsterite. $(4H)_{Si}^{X}$ is always favoured over $(2H)_{Mg}^{X}$ even with 10 wt. ppm water because at low pressures (which favour $(2H)_{Mg}^{X}$) the temperature is also low which favours $(4H)_{Si}^{X}$. As depth increaseds pressure increases and there is a sharp decline in [HMg]. While there is an increase in [HSi] with depth this increase is negligible compared to the concentration at 0 km and so in the absence of other defects [HSi] is steady throughout the upper mantle.

The presence of Al and Ti changes this picture. Figure 7 shows the distribution of these products along the same geotherm but with Al and Ti added. The concentration of both Al and Ti was set to a realistic distribution across the mantle using Equation 13 from De Hoog et al. (2010) (values are given in Table S10) such that the concentration of Al and Ti decreases with depth.

In the presence of Al and Ti we find that at shallow depths $\{Ti_{Mg}^{\cdot\cdot}(2H)_{Si}^{''}\}$ is the most prominent defect except with large amounts of water (>~500 wt. ppm) when $(4H)_{Si}^{X}$ is the prominent defect throughout the upper mantle. With increasing depth each of the 3 important hydrated defects change in different ways. [HMg] initially increases slightly with depth (due to increased temperature favouring $(2H)_{Mg}^{X}$ over $\{Ti_{Mg}^{\cdot\cdot}(2H)_{Si}^{''}\}$), peaking at ~100 km for 10 wt. ppm water, ~50 km for 100 wt. ppm water and 0 km for 1000 wt. ppm water, before decreasing in concentration sharply beyond this point. [HTi] decreases throughout the upper mantle. Initially [HTi] decreases slowly up to around the same point that [HMg] peaks before decreasing sharply. [HSi] initially increases sharply with depth as the increased pressure favours it over the other two defects before reaching a point where $(4H)_{Si}^{X}$ is the most prominent defect and it becomes essentially unchanged with depth, mimicking the behaviour seen in Ti and Al-free forsterite in Figure S4. The depth at which this change in behaviour occurs is shown in Figure 8 and is ~200 km for 1 wt. ppm, ~150 km for 10 wt. ppm, ~100 km

for 100 wt. ppm and 0 km for 1000 wt. ppm water. Thus in shallower drier areas of the upper mantle [HSi] increases sharply with depth but in wetter areas it is consistent with depth.

The changes between Figure 7 and S4 are induced by Ti and not by Al as demonstrated above. The concentration of Ti in the sample is important only if the Ti concentration is low compared to the water concentration in which case $\{Ti^{\cdot\cdot}_{Mg}(2H)''_{Si}\}$ will saturate and be lower than predicted here. Figure S5 shows the same plot as Figure 7 but with a constant (500 wt. ppm) amount of TiO_2 and Al_2O_3. Figure S5 and 7 are nearly identical. This is because at shallow depths, where Ti makes a large difference to the distribution of water, there is large amounts of Ti in both our geological distribution in Fig 7 and in our fixed Ti-rich trace in S5**.** At deep depths where there is large amounts of Ti in Figure S5 and small amounts in the geological distribution in Figure 7 $(4H)^X_{Si}$ dominates regardless of Ti concentration. Thus in shallow and dry areas of the upper mantle Ti concentration (relative to water concentration) is important but in deep and/or wet areas of the upper mantle Ti concentration levels are irrelevant for the main distribution of water in forsterite. Figure S5 contains the highest level of Ti that is likely present in the upper mantle and real samples are likely somewhere between this and Figure 7. Thus $(4H)^X_{Si}$ is likely always the dominant water product in mantle forsterite and steady throughout the upper mantle except for the shallowest, driest and most Ti rich forsterites.

[HMg]

Increasing the concentration of $(2H)^X_{Mg}$ will primarily have effects on the diffusion of Mg (Fei et al., 2018)**,** the diffusion of hydrogen and the conductivity in regions above ~900 C and with high water concentrations- ie most of the upper mantle (Demouchy and Bolfan-Casanova, 2016, Demouchy and Mackwell, 2006, Yoshino et al., 2017, Novella et al., 2017). We find that with small amounts of water (with some Ti and Al) [HMg] initially rises and then falls sharply after

444 a depth defined by temperature, water and Ti concentration. With large amounts of water
445 [HMg] decreases slowly around the first 100 km of the upper mantle and then quickly.

446 Under young oceanic plates conductivity increases on the order of a magnitude have been seen
447 peaking at around 70-120 km (Baba et al., 2006, Baba et al., 2010). If these regions contain
448 water this conductivity spike could be explained by $(2H)_{Mg}^{X}$. The conductivity increase seen
449 in these regions is also strongly anisotropic which can also be explained by an increase of
450 $(2H)_{Mg}^{X}$ as increasing the Mg diffusion rate by adding vacancies should lead to anisotropic
451 diffusion and thus conduction.

452 In the general upper mantle conductivity either increases sharply up to 100 km depth and then
453 slowly afterwards in oceanic mantle or continually increases at similar rates in continental
454 mantle (Sun et al., 2019). While conductivity will generally increase as you descend into the
455 mantle simply due to the increased temperature if conductivity in this region is tied to Mg
456 diffusion rates which are tied to water one would expect, based on this work, a large decrease
457 in conductivity with depth which is not observed in reality.

458 There are three reasons why such a signal may not be observed. First the relationship of
459 $(2H)_{Mg}^{X}$ to Mg diffusion rates and conductivity may not be straightforward. A relatively
460 immobile $(2H)_{Mg}^{X}$ could explain why there is no large decrease in conductivity with depth.
461 Alternatively Mg diffusion in forsterite might not be the controlling factor for forsterite in these
462 conditions with polaron or grain boundary diffusion or other mechanisms actually being
463 dominant. Second the increased temperature of the deep upper mantle which will increase
464 conductivity may overweigh the decreases caused by a shrinking [HMg]- the diffusivity of
465 $(2H)_{Mg}^{X}$ needs to be known to address this point. Third it may be that Mg diffusion controls
466 the conductivity of forsterite but that the upper mantle is very dry. A dry upper mantle would

only have small changes to Mg diffusion regardless of the relative prominence of $(2H)_{Mg}^{X}$ and thus no conductivity decreases with depth.

[HSi]

Increasing the concentration of $(4H)_{Si}^{X}$ will have large effects as Si is the slowest diffusing species in olivine (Chakraborty, 2010) and thus is assumed to control its diffusion-mediated creep, both in diffusion creep and dislocation creep regimes where they are climb limited (see Demouchy and Bolfan-Casanova (2016) for a review). Thus adding water to forsterite, particularly at high pressure, should increase its creep rate and cause it to weaken. This "hydrolytic weakening" has been observed in both diffusion and dislocation creep regimes (Mei and Kohlstedt, 2000a, Mei and Kohlstedt, 2000b, Karato et al., 1986, Demouchy et al., 2012, Girard et al., 2013a, Tielke et al., 2018, Jung and Karato, 2001, Hirth and Kohlstedt, 2003, Mackwell et al., 1985)**,** as has an increase in the silicon diffusion rate (Costa and Chakraborty, 2008, Fei et al., 2013) with these two mechanisms hypothesised as linked (Fei et al., 2016)**.** The strain rate of forsterite has been found to increase in the presence of water from around half an order of magnitude (Mei and Kohlstedt, 2000a, Mei and Kohlstedt, 2000b, Fei et al., 2013, Girard et al., 2013b, Tielke et al., 2018, Demouchy et al., 2012, Umemoto et al., 2011) to a couple of orders of magnitude (Costa and Chakraborty, 2008, Karato et al., 1986, Jung and Karato, 2001) with these differences often explained by experimental differences in strain rates, compositions and water content with grain boundary water likely an important confounder of results. The two works at the highest pressures (4-8 GPa (Fei et al., 2013, Girard et al., 2013a)) where [HSi] should be the largest found the lowest weakening which could be evidence that either [HSi] is not important in Si diffusion or that Si diffusion is not important in the rheological strength of forsterite (which would also explain the difference between direct strength measurements and those from Si diffusion measurements) but may be evidence that other studies have overestimated the weakening effects.

Determining the water exponent of hydrolytic weakening will give insight into its weakening mechanism. The exponent of water's effect has been measured as 1/3 (Fei et al., 2013), 0.2-1 (Costa and Chakraborty, 2008), ~1.2 (Hirth and Kohlstedt, 2003, Tielke et al., 2018) and 0.2 (Mackwell et al., 1985) though in all cases the experimental data is scattered and could be plausibly fit with different exponents. In Fei et al. (2016) an exponent of 1/3 was explained for Si diffusion by co-diffusion of Si and O using the exponents of Kohlstedt (2006) and a charge balance regime of $[(OH)_O^{\cdot}] = 2[V_{Mg}'']$ with V_{Si}'''' having an exponent of 2/3 and with $(4H)_{Si}^{X}$ being immobile. We find this unlikely for a few reasons. We find that the charge balance regime is either $[p^{\bullet}] = 2[H_{Me}']$ or $[p^{\bullet}] = 4[H_{Si}']$ and thus V_{Si}'''' will be either unchanged by water content (r=0 in the ideal case) or somewhat decreased due to entropy concerns (we find r for V_{Si}'''' to be ~0- -0.5 in the conditions of the experiment 8 GPa, 1600-1800 K). Thus an immobile $(4H)_{Si}^{X}$ would lead to a decrease in Si diffusion rates with water. Even in the limit of the charge balance $[(OH)_O^{\cdot} = 2[V_{Mg}'']$ the measured exponent of 1/3 is against $[H_2O]_{bulk}$ rather than water fugacity (Equation 5 rather than 4) and thus the perfect exponent for V_{Si}'''' would be 2 and not 2/3. If $(4H)_{Si}^{X}$ is the dominant water structure and $[p^{\bullet}] = 4[H_{Si}']$ is the charge balance in these products as we predict then the exponent of both V_{Si}'''' and $V_O^{\bullet\bullet}$ should be 0 in the ideal case and that of $(4H)_{Si}^{X}$ should be 1 with the actual exponent of V_{Si}'''' and $V_O^{\bullet\bullet}$ being slightly negative. Determining the water exponent of Si diffusion is impossible in this work without knowing the diffusivity of dry and wet Si vacancies but a Si diffusion exponent of ~1/3-2/3 at high pressure (where the $(4H)_{Si}^{X}$ exponent is ~1) or ~1.2 at lower pressures (where the $(4H)_{Si}^{X}$ exponent is ~2) makes sense if Si diffusion is a mixture of these two species as it would place the exponent roughly halfway between these two species. Thus we propose that the water exponent of Si diffusion is variable and is low (~1/3) at high pressure but higher at low pressure (<~1 GPa depending upon temperature and water content).

If Si diffusion is responsible for weakening of forsterite then the same exponent should also hold for olivine strength.

Such an effect has been seen in olivine creep strength in Karato and Jung (2003) where it was observed that in wet olivine creep strength decreases rapidly with pressure below ~1 GPa but slowly above this. This is evidence of a changing exponent at around 1 GPa which makes sense if creep rate is tied to Si diffusion which is tied to [HSi] as around 1 GPa you change from a $(2H)^{X}_{Mg}$ dominated region to one dominated by $(4H)^{X}_{Si}$ and change the exponent of $(4H)^{X}_{Si}$ from 2 to 1.

We predict such changes to occur in the upper mantle. As can be seen in Figure 8 there are two regions for [HSi] in the upper mantle reflective of these two charge balance regions. In the shallow upper mantle and in drier rocks there is a region of sharp increase in [HSi] with depth, this is a region where $(2H)^{X}_{Mg}$ or $Ti^{\bullet\bullet}_{Mg}(2H)^{\prime\prime}_{Si}$ dominates. In this region there should be sharp increases in [HSi] with depth and thus large changes in olivine strength with depth. For 100 wt. ppm water [SiH] increases by over an order of magnitude over the first 150 km, for 10 wt. ppm water [SiH] increases by 2.5 orders over the first 200 km of the upper mantle and olivine strength should lower accordingly. The second region is one where $(4H)^{X}_{Si}$ is the dominant product and in this region [HSi] is nearly insensitive to depth. It increases slightly with depth in all cases but this change is so small as to be negligible. Across this region the strength of wet forsterite should be fixed with depth. This region starts earlier in the mantle with more water (~200 km with 10 wt. ppm, ~150 km with 100 wt. ppm, ~0 km with 1000 wt. ppm) such that very wet crystals should have consistent strength throughout the upper mantle. These results suggest, therefore, that drier shallower olivines could have strengths that vary by orders of magnitude with depth and that olivine cannot be treated as a structure with a fixed

strength throughout the upper mantle unless it is very wet such that [HSi] does not very with depth or extremely dry such that water does not change the strength at all.

In conclusion we find that water distribution in lower mantle forsterite is mainly a function of depth. Lower water concentrations and higher temperatures favour $(2H)^{X}_{Mg}$ while higher Ti concentrations favour $\{Ti^{\cdot\cdot}_{Mg}(2H)^{\prime\prime}_{Si}\}$ but pressure overwhelmingly favours $(4H)^{X}_{Si}$ and this becomes the key factor descending into the lower mantle**.** In drier rocks $(2H)^{X}_{Mg}$ or $\{Ti^{\cdot\cdot}_{Mg}(2H)^{\prime\prime}_{Si}\}$ can be the dominant water defect and peak in concentration around 100-150 km suggesting a maximum Mg diffusion rate and conductivity around this depth. In these drier rocks [HSi] increases steadily across this range of depths and thus the rocks should become weaker as they increase in depth. In very wet rocks $(4H)^{X}_{Si}$ is the dominant water carrying phase throughout and thus there should be consistent Si diffusion rates and strength throughout the upper mantle. Water in forsterite is highly sensitive to the environmental conditions and so universal laws are likely to fail except outside the conditions in which they were created.

BABA, K., CHAVE, A. D., EVANS, R. L., HIRTH, G. & MACKIE, R. L. 2006. Mantle dynamics beneath the East Pacific Rise at 17 degrees S: Insights from the Mantle Electromagnetic and Tomography (MELT) experiment. *Journal of Geophysical Research-Solid Earth,* 111.

BABA, K., UTADA, H., GOTO, T.-N., KASAYA, T., SHIMIZU, H. & TADA, N. 2010. Electrical conductivity imaging of the Philippine Sea upper mantle using seafloor magnetotelluric data. *Physics of the Earth and Planetary Interiors,* 183**,** 44-62.

BALAN, E., INGRIN, J., DELATTRE, S., KOVACS, I. & BLANCHARD, M. 2011. Theoretical infrared spectrum of OH-defects in forsterite. *European Journal of Mineralogy,* 23**,** 285-292.

BERRY, A. J., HERMANN, J., O'NEILL, H. S. C. & FORAN, G. J. 2005. Fingerprinting the water site in mantle olivine. *Geology,* 33**,** 869-872.

BERRY, A. J., O'NEILL, H. S. C., HERMANN, J. & SCOTT, D. R. 2007a. The infrared signature of water associated with trivalent cations in olivine. *Earth and Planetary Science Letters,* 261**,** 134-142.

BERRY, A. J., WALKER, A. M., HERMANN, J., O'NEILL, H. S., FORAN, G. J. & GALE, J. D. 2007b. Titanium substitution mechanisms in forsterite. *Chemical Geology,* 242**,** 176-186.

BLANCHARD, M., INGRIN, J., BALAN, E., KOVACS, I. & WITHERS, A. C. 2017. Effect of iron and trivalent cations on OH defects in olivine. *American Mineralogist,* 102**,** 302-311.

BRAITHWAITE, J. S., SUSHKO, P. V., WRIGHT, K. & CATLOW, C. R. A. 2002. Hydrogen defects in Forsterite: A test case for the embedded cluster method. *Journal of Chemical Physics,* 116**,** 2628-2635.

BRAITHWAITE, J. S., WRIGHT, K. & CATLOW, C. R. A. 2003. A theoretical study of the energetics and IR frequencies of hydroxyl defects in forsterite. *Journal of Geophysical Research-Solid Earth,* 108.

BRODHOLT, J. P. & REFSON, K. 2000. An ab initio study of hydrogen in forsterite and a possible mechanism for hydrolytic weakening. *Journal of Geophysical Research-Solid Earth,* 105**,** 18977-18982.

CHAKRABORTY, S. 2010. Diffusion Coefficients in Olivine, Wadsleyite and Ringwoodite. *In:* ZHANG, Y. X. & CHERNIAK, D. J. (eds.) *Diffusion in Minerals and Melts.*

CLARK, S. J., SEGALL, M. D., PICKARD, C. J., HASNIP, P. J., PROBERT, M. J., REFSON, K. & PAYNE, M. C. 2005. First principles methods using CASTEP. *Zeitschrift fuer Kristallographie,* 220**,** 567-570.

COSTA, F. & CHAKRABORTY, S. 2008. The effect of water on Si and O diffusion rates in olivine and implications for transport properties and processes in the upper mantle. *Physics of the Earth and Planetary Interiors,* 166**,** 11-29.

DE HOOG, J. C. M., GALL, L. & CORNELL, D. H. 2010. Trace-element geochemistry of mantle olivine and application to mantle petrogenesis and geothermobarometry. *Chemical Geology,* 270**,** 196-215.

DEMOUCHY, S. & BOLFAN-CASANOVA, N. 2016. Distribution and transport of hydrogen in the lithospheric mantle: A review. *Lithos,* 240**,** 402-425.

DEMOUCHY, S. & MACKWELL, S. 2006. Mechanisms of hydrogen incorporation and diffusion in iron-bearing olivine. *Physics and Chemistry of Minerals,* 33**,** 347-355.

DEMOUCHY, S., TOMMASI, A., BAROU, F., MAINPRICE, D. & CORDIER, P. 2012. Deformation of olivine in torsion under hydrous conditions. *Physics of the Earth and Planetary Interiors,* 202**,** 56-70.

FEI, H., KOIZUMI, S., SAKAMOTO, N., HASHIGUCHI, M., YURIMOTO, H., MARQUARDT, K., MIYAJIMA, N., YAMAZAKI, D. & KATSURA, T. 2016. New constraints on upper mantle creep mechanism inferred from silicon grain-boundary diffusion rates. *Earth and Planetary Science Letters,* 433**,** 350-359.

FEI, H., WIEDENBECK, M., YAMAZAKI, D. & KATSURA, T. 2013. Small effect of water on upper-mantle rheology based on silicon self-diffusion coefficients. *Nature,* 498**,** 213-+.

FEI, H. Z., KOIZUMI, S., SAKAMOTO, N., HASHIGUCHI, M., YURIMOTO, H., MARQUARDT, K., MIYAJIMA, N. & KATSURA, T. 2018. Mg lattice diffusion in iron-free olivine and implications to conductivity anomaly in the oceanic asthenosphere. *Earth and Planetary Science Letters,* 484**,** 204-212.

GIRARD, J., CHEN, J., RATERRON, P. & HOLYOKE, C. W., III 2013a. Hydrolytic weakening of olivine at mantle pressure: Evidence of 100 (010) slip system softening from single-crystal deformation experiments. *Physics of the Earth and Planetary Interiors,* 216**,** 12-20.

GIRARD, J., CHEN, J., RATERRON, P. & HOLYOKE III, C. 2013b. Hydrolytic weakening of olivine at mantle pressure: Evidence of [100](010) slip system softening from single-crystal deformation experiments. *Physics of the Earth and Planetary Interiors,* 216**,** 12-20.

HAIBER, M., BALLONE, P. & PARRINELLO, M. 1997. Structure and dynamics of protonated Mg2SiO4: An ab-initio molecular dynamics study. *American Mineralogist,* 82**,** 913-922.

HIRSCHMANN, M. M. 2006. Water, melting, and the deep Earth H(2)O cycle. *Annual Review of Earth and Planetary Sciences.*

HIRTH, G. & KOHLSTEDT, D. L. 2003. Rheology of the Upper Mantle and the Mantle Wedge: A view from the Experimentalists. *Geophysical Monograph Series,* 138**,** 83-105.

INGRIN, J., KOVACS, I., DELOULE, E., BALAN, E., BLANCHARD, M., KOHN, S. C. & HERMANN, J. 2014. Identification of hydrogen defects linked to boron substitution in synthetic forsterite and natural oliyine. *American Mineralogist,* 99**,** 2138-2141.

ISAAK, D. G., ANDERSON, O. L., GOTO, T. & SUZUKI, I. 1989. ELASTICITY OF SINGLE-CRYSTAL FORSTERITE MEASURED TO 1700-K. *Journal of Geophysical Research-Solid Earth and Planets,* 94**,** 5895-5906.

JUNG, H. & KARATO, S. 2001. Water-induced fabric transitions in olivine. *Science,* 293**,** 1460-1463.

KARATO, S., JUNG, H., KATAYAMA, I. & SKEMER, P. 2008. Geodynamic significance of seismic anisotropy of the upper mantle: New insights from laboratory studies. *Annual Review of Earth and Planetary Sciences.*

KARATO, S. I. & JUNG, H. 2003. Effects of pressure on high-temperature dislocation creep in olivine. *Philosophical Magazine,* 83**,** 401-414.

KARATO, S. I., PATERSON, M. S. & FITZ GERALD, J. D. 1986. RHEOLOGY OF SYNTHETIC OLIVINE AGGREGATES - INFLUENCE OF GRAIN-SIZE AND WATER. *Journal of Geophysical Research-Solid Earth and Planets,* 91**,** 8151-8176.

KOHLSTEDT, D. L. 2006. The role of water in high-temperature rock deformation. *In:* KEPPLER, H. & SMYTH, J. R. (eds.) *Water in Nominally Anhydrous Minerals.* Chantilly: Mineralogical Soc Amer & Geochemical Soc.

KUNG, J., LI, B. S., UCHIDA, T., WANG, Y. B., NEUVILLE, D. & LIEBERMANN, R. C. 2004. In situ measurements of sound velocities and densities across the orthopyroxene -> high-pressure clinopyroxene transition in MgSiO3 at high pressure. *Physics of the Earth and Planetary Interiors,* 147**,** 27-44.

LE LOSQ, C., JOLLANDS, M. C., TOLLAN, P. M. E., HAWKINS, R. & O'NEILL, H. S. C. 2019. Point defect populations of forsterite revealed by two-stage metastable hydroxylation experiments. *Contributions to Mineralogy and Petrology,* 174.

LEMAIRE, C., KOHN, S. C. & BROOKER, R. A. 2004. The effect of silica activity on the incorporation mechanisms of water in synthetic forsterite: a polarised infrared spectroscopic study. *Contributions to Mineralogy and Petrology,* 147**,** 48-57.

MACKWELL, S. J., KOHLSTEDT, D. L. & PATERSON, M. S. 1985. THE ROLE OF WATER IN THE DEFORMATION OF OLIVINE SINGLE-CRYSTALS. *Journal of Geophysical Research-Solid Earth and Planets,* 90**,** 1319-1333.

MATVEEV, S., O'NEILL, H. S., BALLHAUS, C., TAYLOR, W. R. & GREEN, D. H. 2001. Effect of silica activity on OH-IR spectra of olivine: Implications for low-aSiO(2) mantle metasomatism. *Journal of Petrology,* 42**,** 721-729.

MEI, S. & KOHLSTEDT, D. L. 2000a. Influence of water on plastic deformation of olivine aggregates 1. Diffusion creep regime. *Journal of Geophysical Research-Solid Earth,* 105**,** 21457-21469.

MEI, S. & KOHLSTEDT, D. L. 2000b. Influence of water on plastic deformation of olivine aggregates 2. Dislocation creep regime. *Journal of Geophysical Research-Solid Earth,* 105**,** 21471-21481.

MOSENFELDER, J. L., DELIGNE, N. I., ASIMOW, P. D. & ROSSMAN, G. R. 2006. Hydrogen incorporation in olivine from 2-12 GPa. *American Mineralogist,* 91**,** 285-294.

MOSENFELDER, J. L., LE VOYER, M., ROSSMAN, G. R., GUAN, Y., BELL, D. R., ASIMOW, P. D. & EILER, J. M. 2011. Analysis of hydrogen in olivine by SIMS: Evaluation of standards and protocol. *American Mineralogist,* 96**,** 1725-1741.

MUIR, J., ZHANG, F. & WALKER, A. M. Submitted. The Controls of Pressure and Water on Highly Anisotropic Mg Diffusion in Forsterite**.,** Preprint available at https://doi.org/10.31223/osf.io/ck3af.

MUIR, J. M. R., JOLLANDS, M., ZHANG, F. W. & WALKER, A. M. 2020. Explaining the dependence of M-site diffusion in forsterite on silica activity: a density functional theory approach. *Physics and Chemistry of Minerals,* 47.

NOVELLA, D., JACOBSEN, B., WEBER, P. K., TYBURCZY, J. A., RYERSON, F. J. & DU FRANE, W. L. 2017. Hydrogen self-diffusion in single crystal olivine and electrical conductivity of the Earth's mantle. *Scientific Reports,* 7**,** 10.

ONO, S. 2008. Experimental constraints on the temperature profile in the lower mantle. *Physics of the Earth and Planetary Interiors,* 170**,** 267-273.

PADRON-NAVARTA, J. A., HERMANN, J. & O'NEILL, H. S. C. 2014. Site-specific hydrogen diffusion rates in forsterite. *Earth and Planetary Science Letters,* 392**,** 100-112.

QIN, T., WENTZCOVITCH, R. M., UMEMOTO, K., HIRSCHMANN, M. M. & KOHLSTEDT, D. L. 2018. Ab initio study of water speciation in forsterite: Importance of the entropic effect. *American Mineralogist,* 103**,** 692-699.

SMYTH, J. R., FROST, D. J., NESTOLA, F., HOLL, C. M. & BROMILEY, G. 2006. Olivine hydration in the deep upper mantle: Effects of temperature and silica activity. *Geophysical Research Letters,* 33.

SPEZIALE, S., ZHA, C. S., DUFFY, T. S., HEMLEY, R. J. & MAO, H. K. 2001. Quasi-hydrostatic compression of magnesium oxide to 52 GPa: Implications for the pressure-volume-temperature equation of state. *Journal of Geophysical Research-Solid Earth,* 106**,** 515-528.

STOCKER, R. L. & SMYTH, D. M. 1978. EFFECT OF ENSTATITE ACTIVITY AND OXYGEN PARTIAL-PRESSURE ON POINT-DEFECT CHEMISTRY OF OLIVINE. *Physics of the Earth and Planetary Interiors,* 16**,** 145-156.

SUN, W., YOSHINO, T., KURODA, M., SAKAMOTO, N. & YURIMOTO, H. 2019. H-D Interdiffusion in Single-Crystal Olivine: Implications for Electrical Conductivity in the Upper Mantle. *Journal of Geophysical Research-Solid Earth,* 124**,** 5696-5707.

TIELKE, J. A., MECKLENBURGH, J., MARIANI, E. & WHEELER, J. 2018. The Influence of Water on the Strength of Olivine Dislocation Slip Systems. *JGR Solid Earth,* 124**,** 6542-6559.

TOLLAN, P. M. E., O'NEILL, H. S. C. & HERMANN, J. 2018. The role of trace elements in controlling H incorporation in San Carlos olivine. *Contributions to Mineralogy and Petrology,* 173.

TOLLAN, P. M. E., SMITH, R., O'NEILL, H. S. C. & HERMANN, J. 2017. The responses of the four main substitution mechanisms of H in olivine to H2O activity at 1050 degrees C and 3 GPa. *Progress in Earth and Planetary Science,* 4.

UMEMOTO, K., WENTZCOVITCH, R. M., HIRSCHMANN, M. M., KOHLSTEDT, D. L. & WITHERS, A. C. 2011. A first-principles investigation of hydrous defects and IR frequencies in forsterite: The case for Si vacancies. *American Mineralogist,* 96**,** 1475-1479.

WALKER, A. M., HERMANN, J., BERRY, A. J. & O'NEILL, H. S. 2007. Three water sites in upper mantle olivine and the role of titanium in the water weakening mechanism. *Journal of Geophysical Research-Solid Earth,* 112**,** 12.

WITHERS, A. C. & HIRSCHMANN, M. M. 2008. Influence of temperature, composition, silica activity and oxygen fugacity on the H2O storage capacity of olivine at 8 GPa. *Contributions to Mineralogy and Petrology,* 156**,** 595-605.

WRIGHT, K. & CATLOW, C. R. A. 1994. A computer simulation study of (OH) defects in olivine. *Physics and Chemistry of Minerals,* 20**,** 515-518.

XUE, X., KANZAKI, M., TURNER, D. & LOROCH, D. 2017. Hydrogen incorporation mechanisms in forsterite: New insights from H-1 and Si-29 NMR spectroscopy and first-principles calculation. *American Mineralogist,* 102**,** 519-536.

YOSHINO, T., ZHANG, B. H., RHYMER, B., ZHAO, C. C. & FEI, H. Z. 2017. Pressure dependence of electrical conductivity in forsterite. *Journal of Geophysical Research-Solid Earth,* 122**,** 158-171.

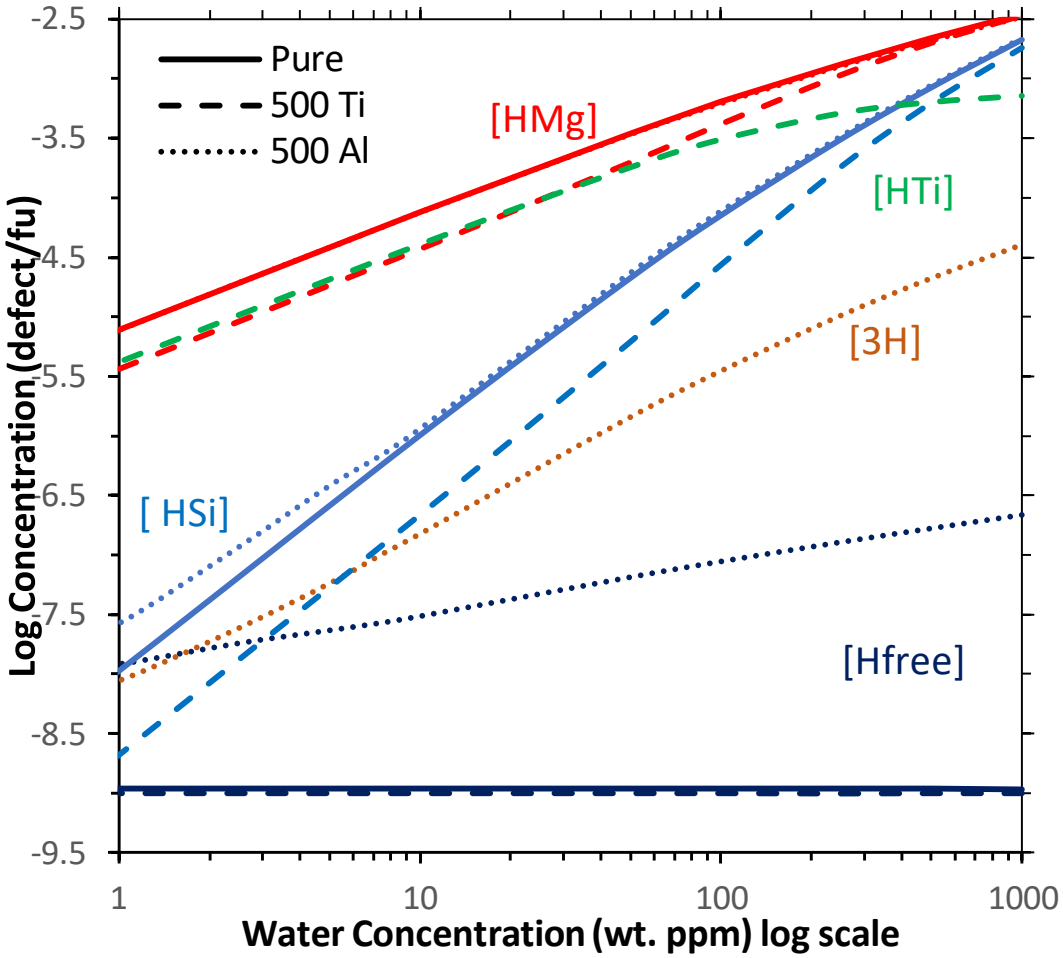

Figure 1: Distribution of products at 2000 K and 0 GPa (corrected) as a function of water content (vs temperature is shown in Figure 2 and vs pressure in Figure 3). Different colours represent different defects and lines different systems (solid line= pure forsterite, dashed line=forsterite+ 500 wt. ppm Al_2O_3, dotted line forsterite+500 wt. ppm TiO_2). Concentrations are defects/f.u. so [Si] has twice as much hydrogen as [Mg] with an equivalent concentration. [Hfree] is nearly identical with and without Ti. [HMg] is identical at this scale for pure and Al-containing forsterite. With increasing water [Si] is favoured. A high pressure graph (10 GPa corrected) is shown in Figure S1 which has very similar trends.

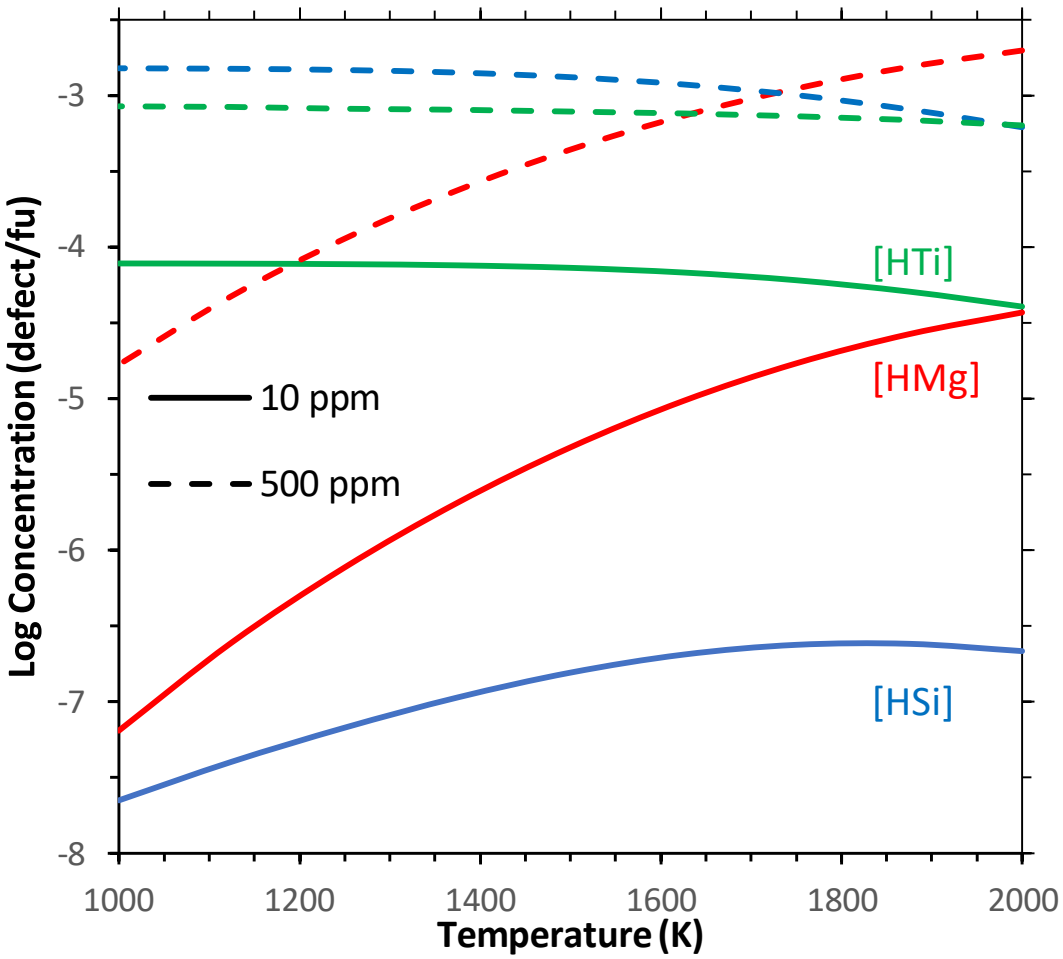

728

729 Figure 2: Distribution of the 3 major products as a function of temperature at 0 GPa
730 (corrected) with 500 wt. ppm Al_2O_3 and TiO_2 with 2 different water contents (10 wt. ppm=
731 solid lines, 500 wt. ppm dashed lines). The same graph at 10 GPa is shown in Figure S2 and
732 for pure forsterite in S3 though trends are similar in both cases just with changes in absolute
733 values.

734

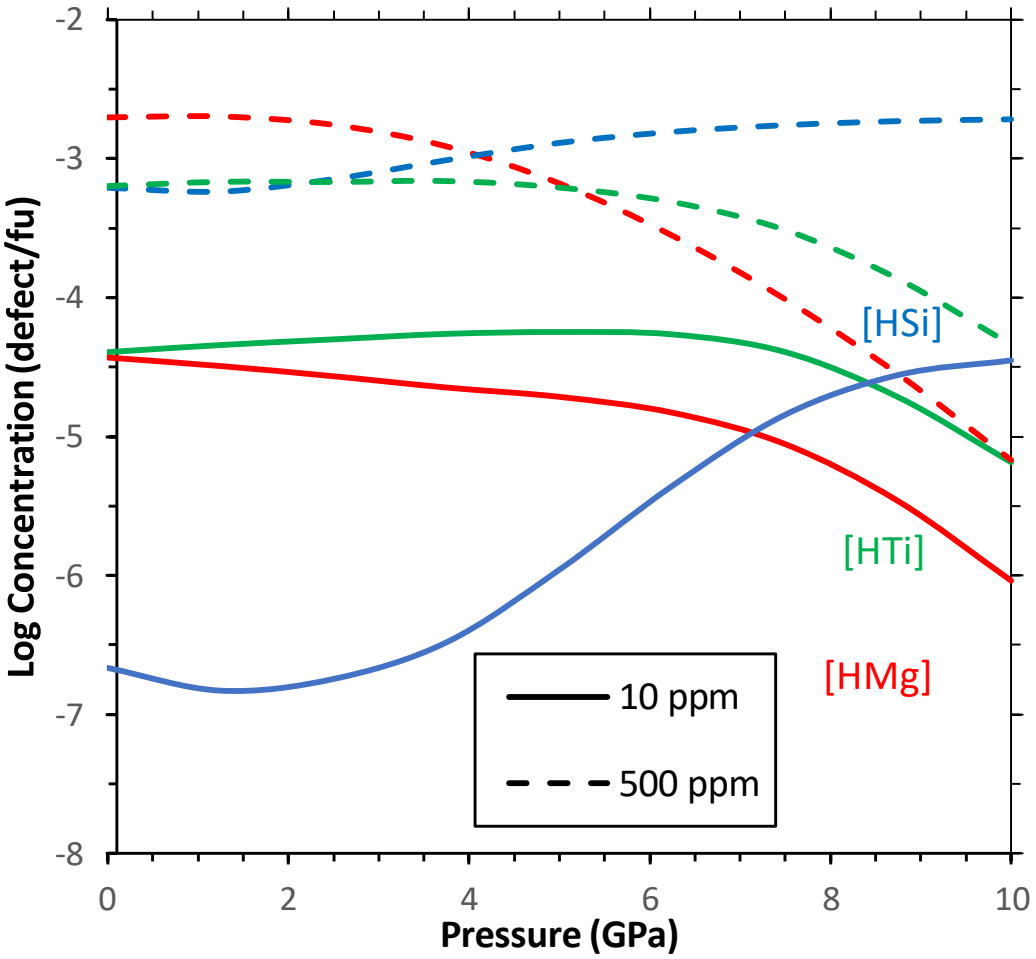

Figure 3: Distribution of the 3 major products as a function of pressure at 2000 K with 500 wt. ppm Al_2O_3 and TiO_2 with 2 different water contents (10 wt. ppm= solid lines, 500 wt. ppm dashed lines). Pressure increases [HSi] but this effect decreases with water content as [HSi] becomes the most prominent defect at all pressures (see Figure 4). [HMg] heavily decreases with pressure, [HTi] increases slightly with pressure and then heavily decreases.

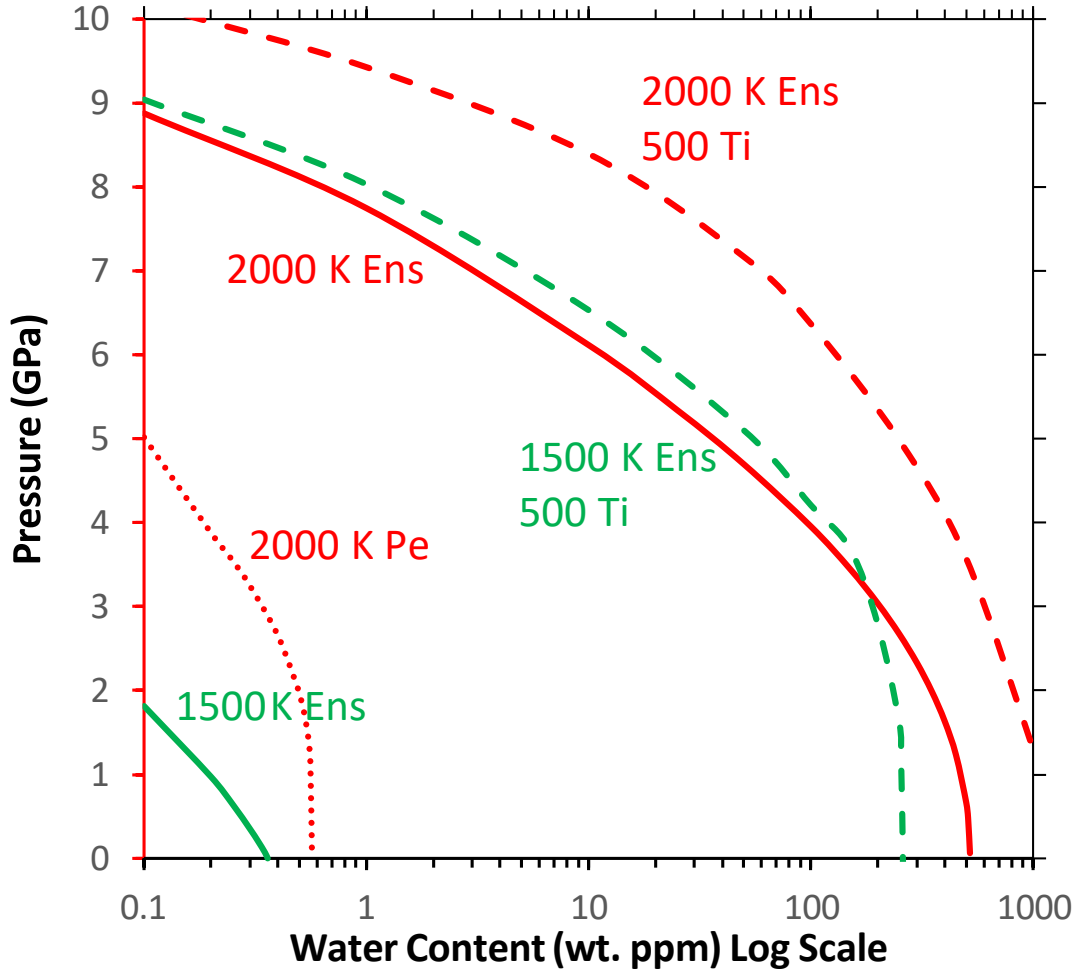

744

745 Figure 4: The crossover pressure as a function of water at fixed T from water being mostly in
746 $(2H)^{X}_{Mg}$ and $\{Ti^{\cdot\cdot}_{Mg}(2H)''_{Si}\}$ to being mostly in $(4H)^{X}_{Si}$ (lowest pressure at which $(4H)^{X}_{Si}$
747 contains over half the water in the system). Shown are a pure forsterite buffered by enstatite
748 (solid line), periclase (dotted line) and a forsterite containing 500 wt. ppm TiO2 buffered by
749 enstatite (dashed line) with colour representing temperature (red=2000, green=1500 K). For
750 1500 K in a pe buffered Ti-free system $(4H)^{X}_{Si}$ contains the majority of the water even at 0
751 GPa as with 1000 K for all conditions.

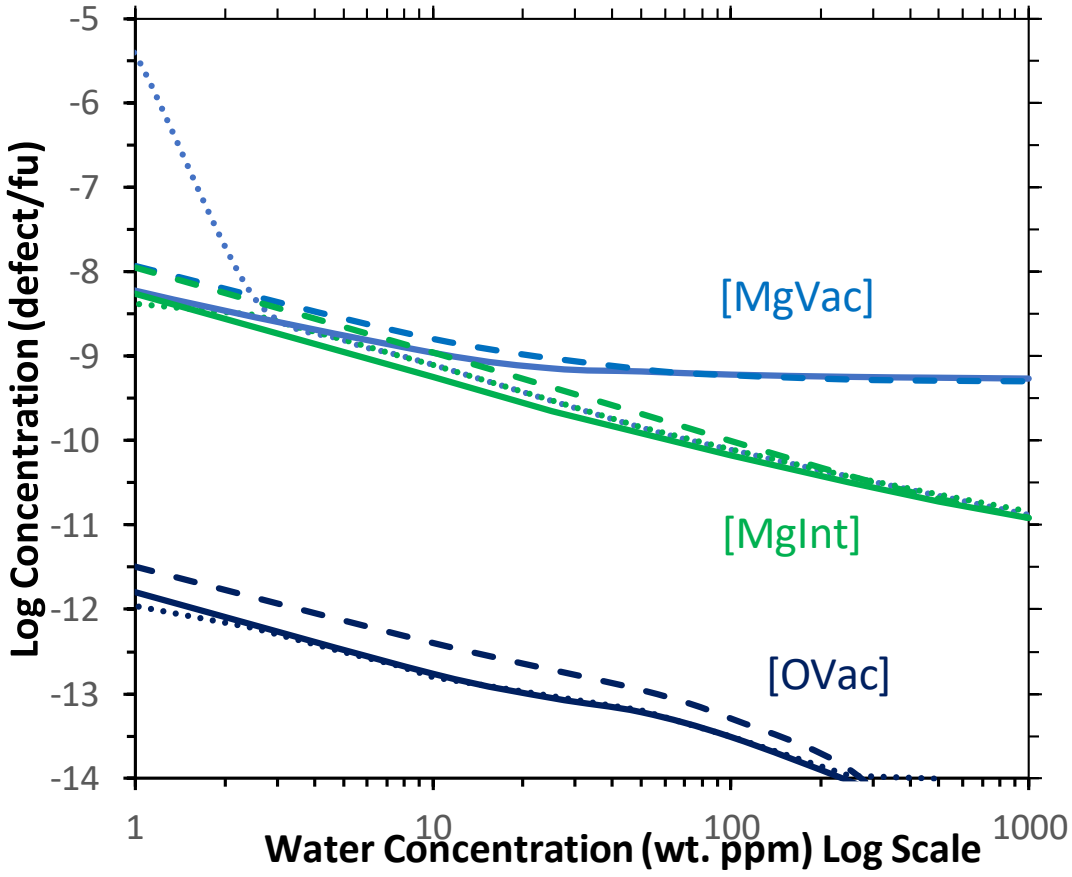

752

753 Figure 5: Plot of the three major intrinsic defects as a function of water concentration at 2000
754 K and 0 GPa (corrected) with three different crystal chemistries (solid line=pure forsterite,
755 dashed line= 500 wt. ppm TiO_2, dotted line= 500 wt. ppm Al_2O_3). The only major difference
756 induced by crystal chemistry is Al induces extra V''_{Mg} due to R8 but this effect is suppressed
757 by high levels of water. The absolute value of these concentrations is less constrained than
758 for intrinsic defects as their concentration is much smaller but the trends with water
759 concentration are better constrained.

760

761

762

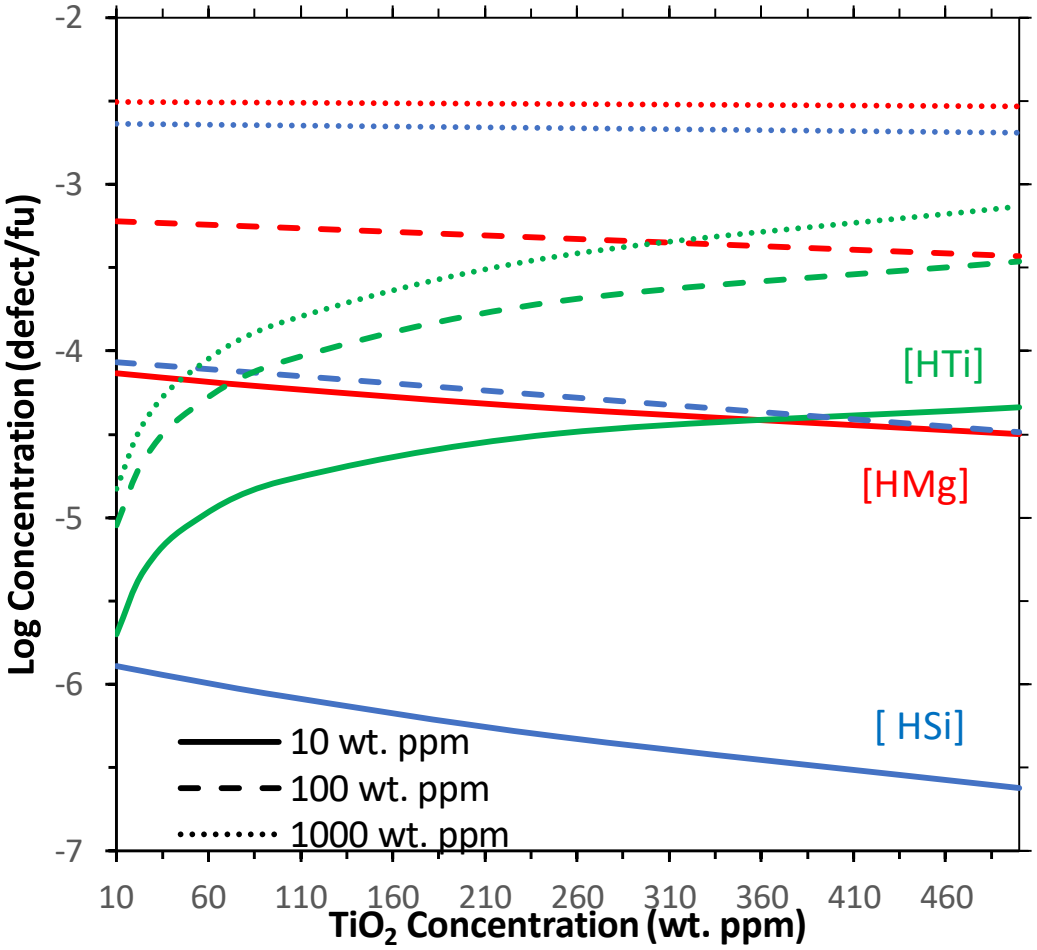

Figure 6: Change in the concentration of the three major defects as a function of Ti content at 2000 K and 0 GPa (corrected) and with different amounts of water (10 wt. ppm solid line, 100 dashed line, 1000 dotted line).

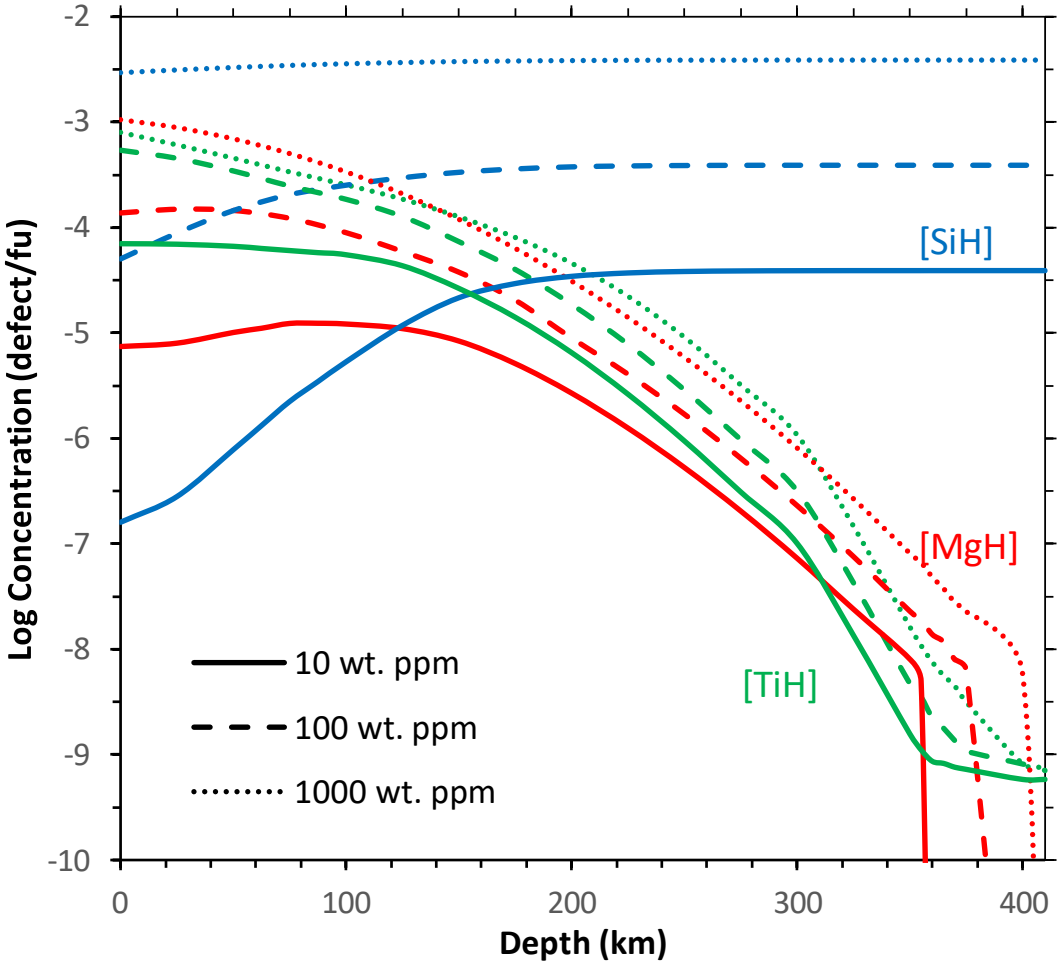

769

770 Figure 7: Plot of the distribution of the three major products along a geotherm with
771 geological distribution of Al and Ti (Table S8) with three different water concentrations (10
772 wt. ppm=solid lines, 100=dashed lines, 1000=dotted lines). For a system with no Ti and Al
773 see Figure S4 and for one with fixed Ti and Al see Figure S5. The general trend is that of
774 increasing $(4H)_{Si}^{X}$ while $(2H)_{Mg}^{X}$ increases and then decreases.

775

776

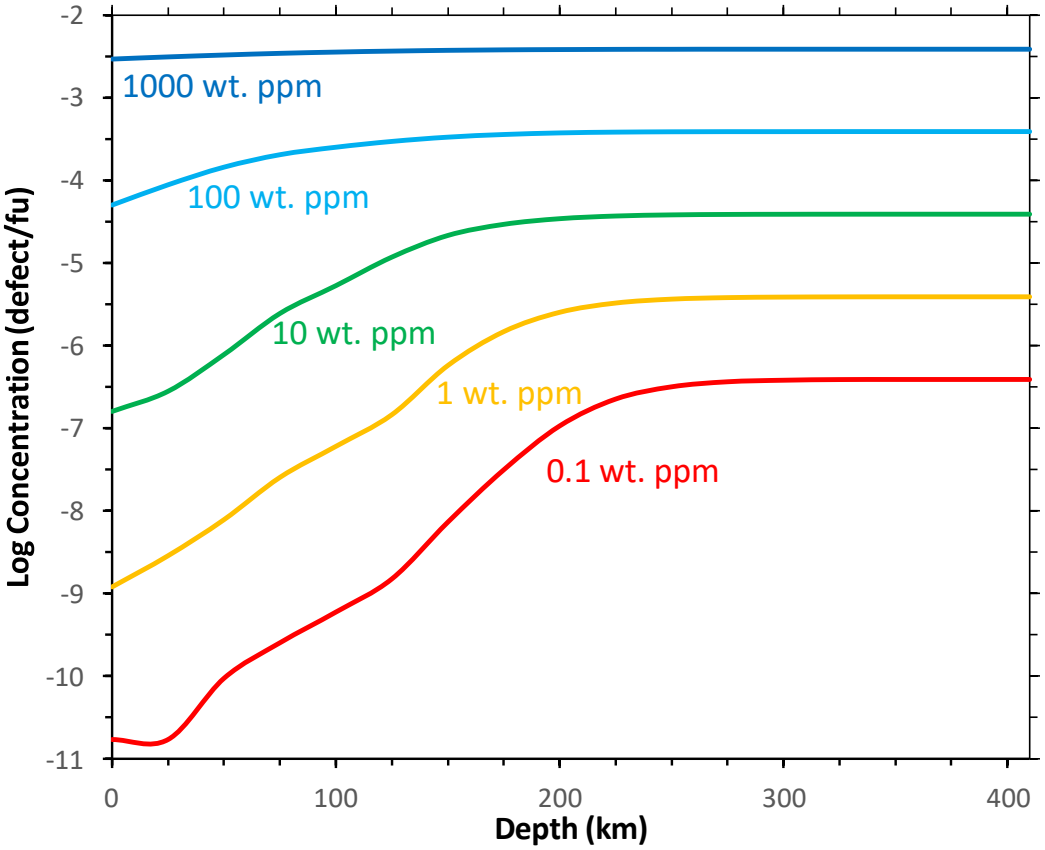

777

778 Figure 8 As Figure 7 but just showing the values for [HSi] with different total water
779 concentrations. With decreasing water [HSi] has a larger increase in concentration over
780 shallower depths.

781

782

	0 GPa			5 GPa			10 GPa		
	1000 K	1500 K	2000 K	1000 K	1500 K	2000 K	1000 K	1500 K	2000 K
R1	-1.337	-2.139	-3.376	-1.336	-2.119	-3.672	-1.337	-1.794	-3.413
R2	0.585	0.564	0.564	0.585	0.564	0.564	0.585	0.565	0.565
R3	6.639	7.772	8.554	6.891	8.700	9.954	7.142	9.627	11.354
R4	-1.031	-1.169	-1.281	-1.045	-1.183	-1.296	-1.006	-1.150	-1.272
R5	-0.421	-0.765	-1.071	-0.282	-0.585	-0.871	0.021	-0.240	-0.513
R6	1.157	1.227	1.142	1.099	1.211	1.124	1.071	1.248	1.178
R7	4.278	4.464	4.472	4.223	4.440	4.388	4.207	4.537	4.490
R8	2.121	2.387	2.560	2.140	2.603	2.842	2.100	2.705	3.023
R11	5.960	6.375	6.918	5.661	6.180	6.877	5.368	5.939	6.747
R22	0.270	0.239	0.231	0.282	0.254	0.258	0.298	0.269	0.278

Table 1: Reaction energies (in eV/f.u) for the hydrated defect reactions (R1-R7) and some other important reactions as a function of pressure and temperature. All other reactions are shown in Table S6.

P Corrected (GPa)	T (K)	Water Conc (wt. ppm)	log 2*[2H]	log [Hint]
0	1000 K	0.001	-7.80	-15.95
		1	-7.30	-15.95
		1000	-6.80	-15.95
0	1500 K	1	-6.57	-11.66
		10	-6.06	-11.68
		100	-5.56	-11.65
0	2000 K	1	-5.51	-9.24
		10	-4.93	-9.24
		100	-4.41	-9.24
10	2000 K	1	-7.94	-14.78
		10	-7.41	-14.78
		100	-6.91	-14.48

Table 2: Concentration (log defect/f.u.) of 2*[2H] and [Hint] (so that they have equal amounts of hydrogen) as a function of pressure and temperature in a system with only 1 reaction R3**.** As can be seen by comparing these values to those in Figure 1 the introduction of other reactions lowers [Hint] except for R7 which raises it a lot. [Hint] is always a lot smaller than [2H] except for extremely small water contents.

			[HMg]	[HSi]	[HTi]	$[V''_{Mg}]$	$[Mg_i^{\bullet\bullet}]$	$[V_O^{\bullet\bullet}]$	$[V''''_{Si}]$proj
Pure	5 GPa	2000 K	0.82	1.63	n/a	0.00	-0.14	-0.84	-0.29
		1500 K	0.60	1.19	n/a	-0.01	-0.01	0.00	-0.01
		1000 K	0.50	1.01	n/a	-0.01	-0.01	0.00	-0.01
	15 GPa	2000 K	0.50	1.00	n/a	0.29	-0.49	-0.49	-0.99
		1500 K	0.50	1.00	n/a	0.26	0.13	0.00	0.26
		1000 K	0.50	1.00	n/a	0.25	0.34	0.00	0.69
TiO_2= 500 ppm Al_2O_3= 500 ppm	5 GPa	2000 K	0.98	1.96	0.61	0.51	-0.56	0.00	-1.12
		1500 K	1.08	2.12	0.49	0.56	-0.82	-0.80	-1.60
		1000 K	1.37	2.65	0.48	0.65	-1.40	-1.51	-2.70
	15 GPa	2000 K	0.51	1.02	0.49	0.26	-0.53	-0.50	-0.39
		1500 K	0.50	1.00	0.47	0.25	-0.19	-0.13	-1.06
		1000 K	0.50	1.00	0.46	0.24	-0.02	0.00	-0.04

Table 3: The water exponent r determined for each of these systems by fitting equation 5 between 10-1000 wt. ppm water. Below 10 wt. ppm water there are sometimes sharp changes in concentration which can strongly distort the exponent. An exponent for V''''_{Si} cannot be reliably determined because it's concentration is small but its concentration is overwhelmingly controlled by R14 and thus its exponent should be roughly double that of V''_{Mg} similarly to how [HSi] is roughly twice [HMg] because it is controlled by R1.

These exponents can be converted into those of equation 4 by assuming an exponent for one of the products. If we assuming [HMg] has a water exponent in Equation 4 then the Equation 5 exponents of the other products can be determined by dividing their exponents by the exponent of [HMg] (first column).

Supplementary Methods for "the distribution of hydrogen in Al and Ti-containing forsterite: A thermodynamic model"

In this section we go into more detail about how we determine energy of different configurations, the different arrangements involved in each defect, the different assumptions involved in our calculation and how our thermodynamic minimiser works.

Determining the energy of defective systems

27 defect forming reactions are presented in the text. We need to find the concentration of defects that provides the lowest possible energy. Each reaction is assigned a reaction vector (x1…x27) between 0 and 1 which determines how far each reaction proceeds to the right between all reactants and all products. For any combination of x1-x27 we can solve for the free energy and the thermodynamic equilibrium is where this free energy is minimised. Solving for the free energy consists of two parts determined as the non-configurational energy and the configurational entropy section:

$\Delta G = \sum_i \Delta E \times x_i - TS_{confa}$ Equation S1

The first half of Equation S1 involves multiplying the energy of each reaction at the appropriate P and T (see Table 1) by its reaction vector to obtain the non-configurational entropy. The second half of Equation S1 involves finding the configurational entropy term S_{confa} for any collection of defects.

1.1) *Configurational Entropy*

The configurational entropy term S_{confa} has many different components and is not straightforward to determine. In short we used the Gibbs entropy formula:

$S = -k_B \sum_j p_j lnp_j$ Equation S2

Where k_B is the Boltzmann constant, j represents a specific configuration of defects and p_j the probability that configuration occurs. A configuration refers to how defects are arranged across the supercell with a set concentration.

The probability of any specific configuration occurring is:

$p_j = \frac{1}{Z} e^{(-U_j/k_B T)}$ Equation S3

Where U_j is the internal energy of each configuration. Z in Equation S3 is the canonical partition function:

$Z = \sum_i e^{(-U_j/k_B T)}$ Equation S4

Strictly speaking S3 and S4 should be calculated with G_j (the free energy of each configuration) rather than U_j (the internal energy of each configuration). This was an approximation made to allow us to calculate the energy of many different configurations quickly as U is much easier to calculate the G. We shall discuss this approximation later. We also do these calculations in the dilute limit with all systems fixed to the forsterite unit cell. This means PV terms do not vary reducing H_j terms to U_j.

At this point we shall define a scheme to group the configurations and bring them down to a calculable number. We shall thus define a configuration as a state where each of the defects of each type is confined to a single type of site. This can be imagined by having a single defect of each type and so the different configurations simply change which site each defect occupies. With our assumption that defects are independent every configuration with the defects confined to a single site is identical and configurations where defects occupy multiple sites are included by the partitioning function. V''_{Mg}, $(1H)'_{Mg}$, $(2H)^X_{Mg}$ and $Al^{\cdot}_{Mg}$ were confined to M1 and M2 sites, V''''_{Si}, Ti^X_{Si}, $(4H)^X_{Si}$, $(3H)'_{Si}$ and Al'_{Si} to Si sites, $Mg_I^{\bullet\bullet}$ to M1 and I2 sites, $V_O^{\bullet\bullet}$ and $H_{Int}^{\cdot}$ to O1, O2 and o3 sites and O_I'' and $Si_I^{\bullet\bullet\bullet\bullet}$ to I1,I2 and T1-T5 sites (which are defined in (Muir et al., 2020)). $\{Ti^{\cdot\cdot}_{Mg}(2H)''_{Si}\}$, $\{2Al^{\bullet}_{Mg}V''_{Mg}\}$ and $\{Al^{\cdot}_{Mg}Al'_{Si}\}$ were calculated as pairs/trios with

each element of the defect confined to a next or second-next neighbour site. All possible geometries of these pairs/trios were tested. For hydrogen atoms in $(2H)_{Mg}^{X}$, $(4H)_{Si}^{X}$, $(1H)_{Mg}'$, $(3H)_{Si}'$ and $(2H)_{Si}''$ defects we considered them bound to an O in the vacancy. We calculated the relative enthalpy of every possible arrangement of hydrogen in these vacancies where an arrangement has each hydrogen bound to a specific O and pointing the hydrogen either in or out of the vacancy. For $H_{Int}^{\bullet}$ the hydrogen was considered bound to an O1, O2 or O3 atom in the bulk. The relative enthalpy of placing a defect in a specific site with a specific hydrogen arrangement was then calculated as a function of pressure as shown in Table S1-S5. We also calculated the enthalpy for all geometric arrangements (with each defect on a next neighbour site with the enthalpies shown in Table S11-S13). For calculating the final free energy of the reactions the most enthalpically stable defect for each arrangement was chosen and its free energy calculated at high temperature. The effect of other arrangements is confined to the configurational entropy term.

All possible configurations (with a defect in a specific site and hydrogen in a specific arrangement) were then tabulated and their relative energy U_j assigned by applying energy penalties determined from the relative enthalpies in Table S1-5. The energy penalty is determined by the difference between the enthalpy of the defect in its current site with its current hydrogen arrangement compared to the enthalpy of the defect in its favored site with its favored hydrogen arrangement. This assumes that the energy of placing and moving a defect around the crystal is independent of the other defects and that defect-defect interaction terms are minimal.

To calculate the degeneracy (W) of each configuration, we must first calculate the degeneracy at each site:

$W=\ln\frac{N!}{a!b!\ldots z!}$ Equation S5

Where N is the total number of sites, and a,b,c…z are the different types of atoms/defects at each site including a final z term, which is simply (N-a-b….-y). To solve this numerically, all defect concentrations were written in terms of defects/mol and then the Stirling approximation was used ($lnn! \cong nln - n$), giving:

$W = NlnN - N - alna + a - blnb + b \ldots - zlnz + z$ Equation S6

Additional degeneracies from hydrogen arrangement degeneracy and the degeneracy of the bound pairs and trios were derived in a similar way added to this term.

Knowing the degeneracy and relative energy of all configurations, the entropy was calculated using Equation S3 but summed across i, where i is simply a sum across every configuration (j) appearing a number of times equal to its degeneracy (W).

In summary, each reaction proceeding to the right produces a set of defects, and then these defects are spread across their different sites according to the energy differences between these sites and the thermodynamic minimum of this distribution. This is determined by the state of every other reaction. An alternative way to consider or calculate this is that (for example) Reaction 5 is 4 reactions- one producing an M1 vacancy and an M1 interstitial, one producing an M2 vacancy /M1 interstitial, one an M1 vacancy /I2 interstitial and one an I2 vacancy /M2 interstitial. However, this will produce the same answer as a single reaction producing a vacancy and an interstitial that are then thermodynamically distributed across their two sites including all the configurational entropy of the different distributions across the sites.

1.2 Testing our assumptions

For this model we assume that the relative energy of placing defects in different sites is not a function of temperature, and that temperature effects occur only in differences between different types of defect (such as V''_{Mg} and $Mg_I^{\cdot\cdot}$) and not between the same defects at different

sites (V''_{Mg} at M1 and M2 for example) as the different Mg sites are similar and thus their vibrational frequencies should be similar.

This was tested for three defects $Mg_I^{\bullet\bullet}$, V''_{Mg} and $(2H)^X_{Mg}$. For the two Mg vacancies (hydrous and anhydrous) it was found that the vibrational entropy difference between the two sites was less than 0.1 eV/defect at 2000 K due to the large similarities between the two sites. This is much lower than the enthalpy differences between these sites and this should be true for most defects which do not have large differences in geometry between M1 and M2 sites. Mg interstitials have very different geometries between M1 and I2 sites and their vibrational entropies are also different. The vibrational entropy difference between these two sites is tabulated in Muir et al. (Submitted) and included in the model and thus for Mg interstitials we use G rather than U in Equation S3 and S4.

We also assume in this model that different arrangements of hydrogen have negligible entropy differences. We tested this with two different arrangements in $(2H)^X_{Mg}$ and $(4H)^X_{Si}$. For Mg we tested configurations 2 and 4 (based on their order in the Table S1) and found the entropy difference was less than 0.085 eV/defect at 2000 K. For Si we tested configurations 1 and 3 (based on their order in Table S2) and found the entropy difference is less than 0.22 eV/defect at 2000 K- this is higher because these configurations are quite different where 4 has a hydrogen outside the vacancy and 1 has all hydrogens inside. This is likely to be the largest entropy difference of all the likely hydrogen arrangements due to the extreme difference in geometry between these two arrangements. For $\{Ti^{\cdot\cdot}_{Mg}(2H)''_{Si}\}$ we tested 4 different arrangements (Row 13 Column 2, R2 C2, R1 C1 and R4 C14 in Table S3) and found differences less than 0.103 eV/defect at 2000 K. These energies are still much lower than the reaction energies and configurational entropy is only a small driver of these reactions so our approximation of using U_j rather G_j is likely reasonably adequate. As shown in Table S7 when we rule out the formation of bound defect pairs we mostly assume that the bound pair

does not have a large increase in favourability with temperature and rely upon enthalpy to determine if they are bound. This assumption was tested for some pairs as shown in Table S7 and was found to be the case.

We also assume that a quasi-harmonic approximation derived via linear displacement at a single q-point is a good measure of the energy of these systems. In Muir et al. (2020) we tested this assumption for dry vacancies and found it to be accurate. While hydrous vacancies have considerable anharmonicities these largely cancel out as previously demonstrated from ringwoodite and bridgmanite which have similar hydrous vacancies **REF RINGWOODITEPAPER.**

1.3 Thermodynamic Minimisation

Once we can determine the energy of any configuration, we need to find which configuration of defects gives the lowest energy. This is a difficult problem as we are dealing with variables that can have values that are many orders of magnitude different, multiple local minimums and a configurational entropy term that has many terms and is difficult to solve analytically. Instead we used a bespoke solver which minimised each variable in turn through brute force and went through the variables multiple times. Such a method relies upon the large energy differences of each of the different reactions (R1-R5). R1 is the most favoured reaction and the progress of reactions R2-R5 has little effect on the progression of R1 because the energy terms involved in R1 are much larger. Thus we solved each reaction in turn from most favoured to least favoured and repeated this until the energy no longer varied. As stated in the text, determining concentrations of defects that are below $1x10^{-20}$ defects/f.u. proved very difficult as we encountered issues with floating points numbers and the precision of our calculations (when the other defects had much higher concentrations) and thus we used this as a baseline cutoff beyond which variables were not minimised. Our minimisation process does not present

a formal solution and may miss a true energy minimum and small variations in the final concentration of the products but should provide a good guide to how different conditions vary the concentration of the water products.

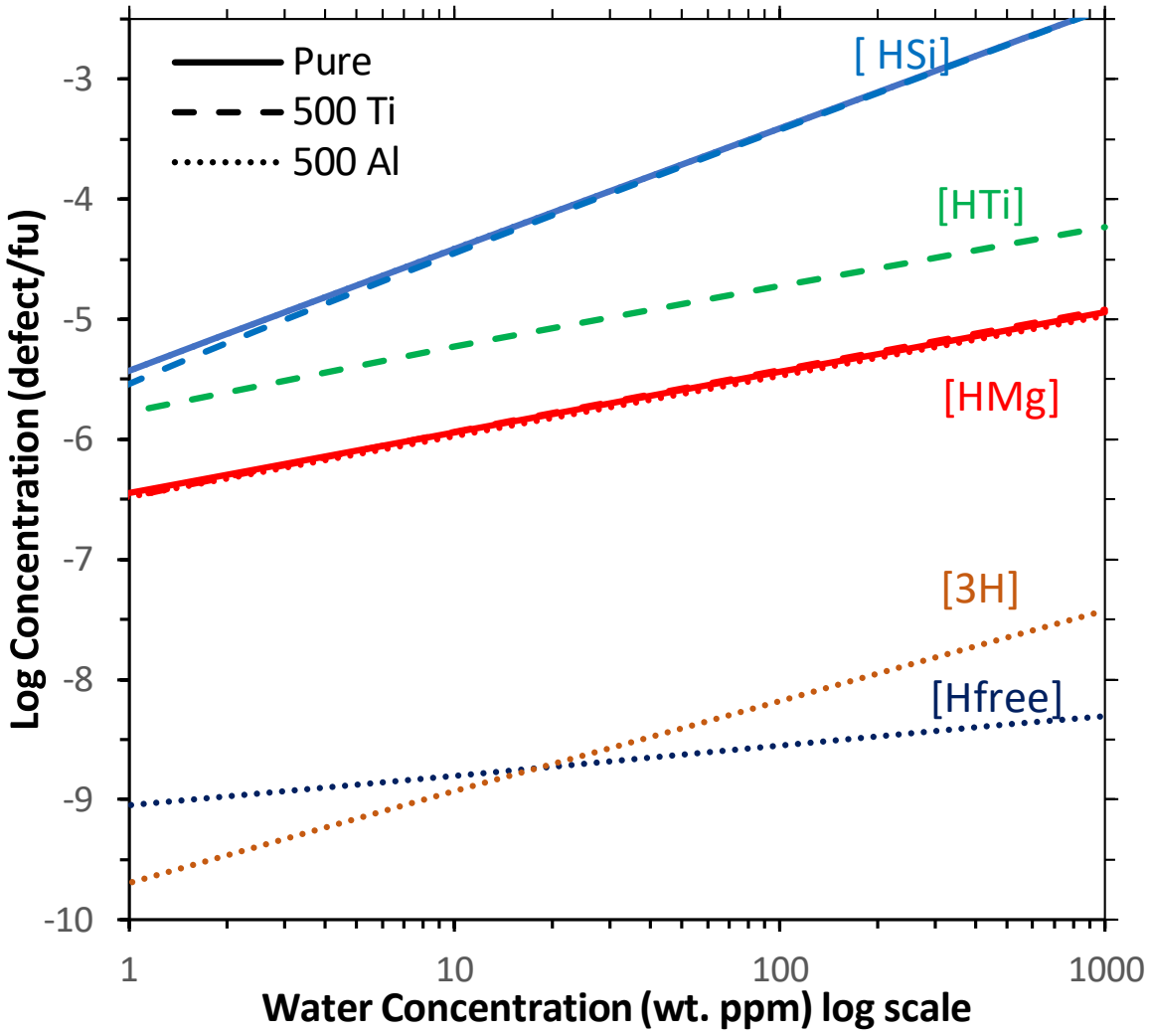

Figure S1 Distribution of products at 2000 K and 10 GPa (corrected) as a function of water content. Different colours represent different defects and lines different systems (solid line= pure forsterite, dashed line=forsterite+ 500 wt. ppm Al_2O_3, dotted line forsterite+500 wt. ppm TiO_2). Concentrations are defects/f.u. so [Si] has twice as much hydrogen as [Mg] with an equivalent concentration. [HSi] and [HMg] is near identical for all three compositions and cannot be distinguished at this scale. With increasing water [HSi] is favoured. [Hfree] is nearly identical with and without Ti and is around -14.25.

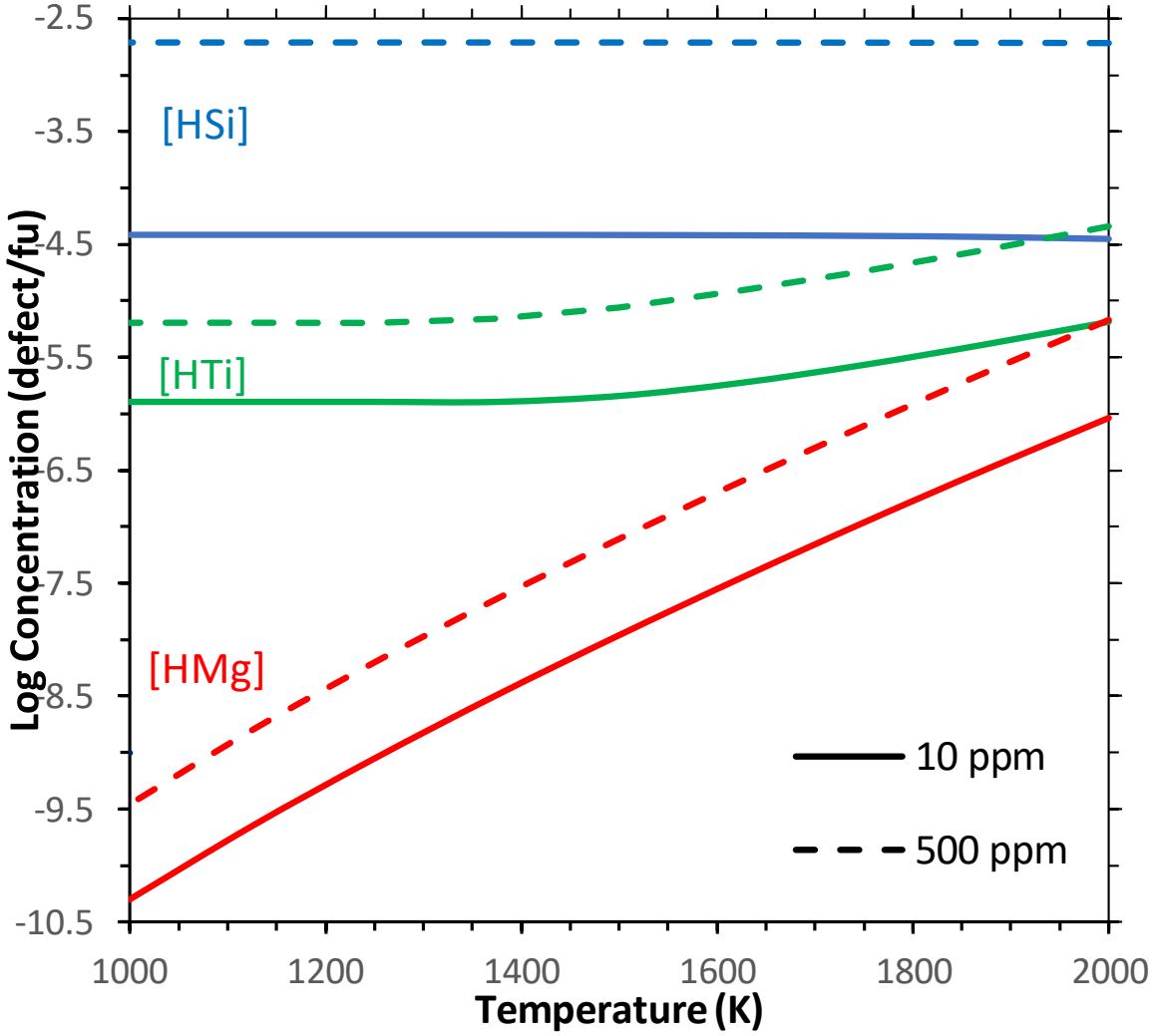

969

970 Figure S2: Distribution of the 3 major products as a function of temperature at 10 GPa
971 (corrected) with 500 wt. ppm Al_2O_3 and TiO_2 with 2 different water contents (10 wt. ppm=
972 solid lines, 500 wt. ppm dashed lines).

973

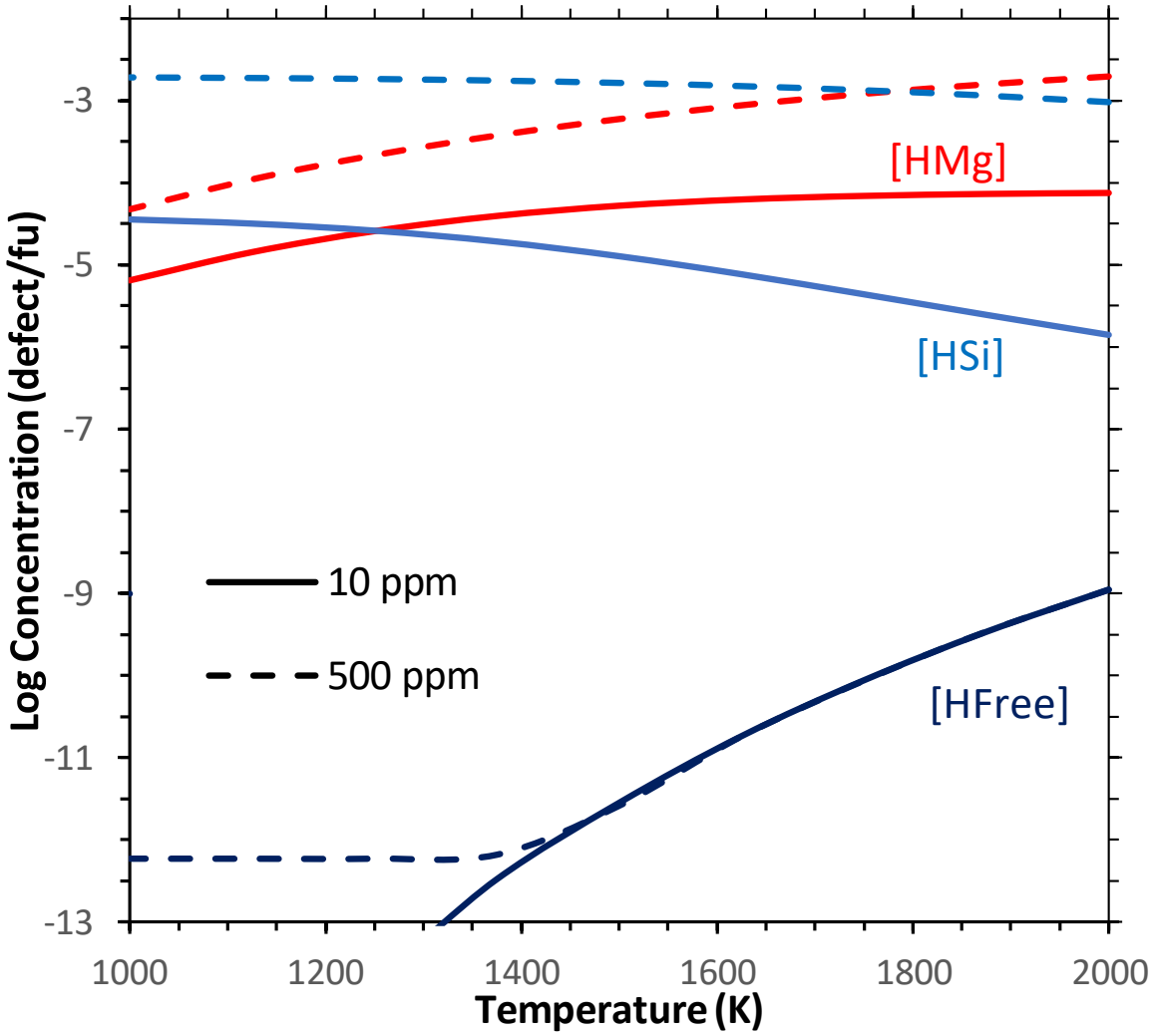

974

975 Figure S3: Distribution of the 3 major products as a function of temperature at 0 GPa (corrected)
976 with pure forsterite and with 2 different water contents (10 wt. ppm= solid lines, 500 wt. ppm
977 dashed lines).

978

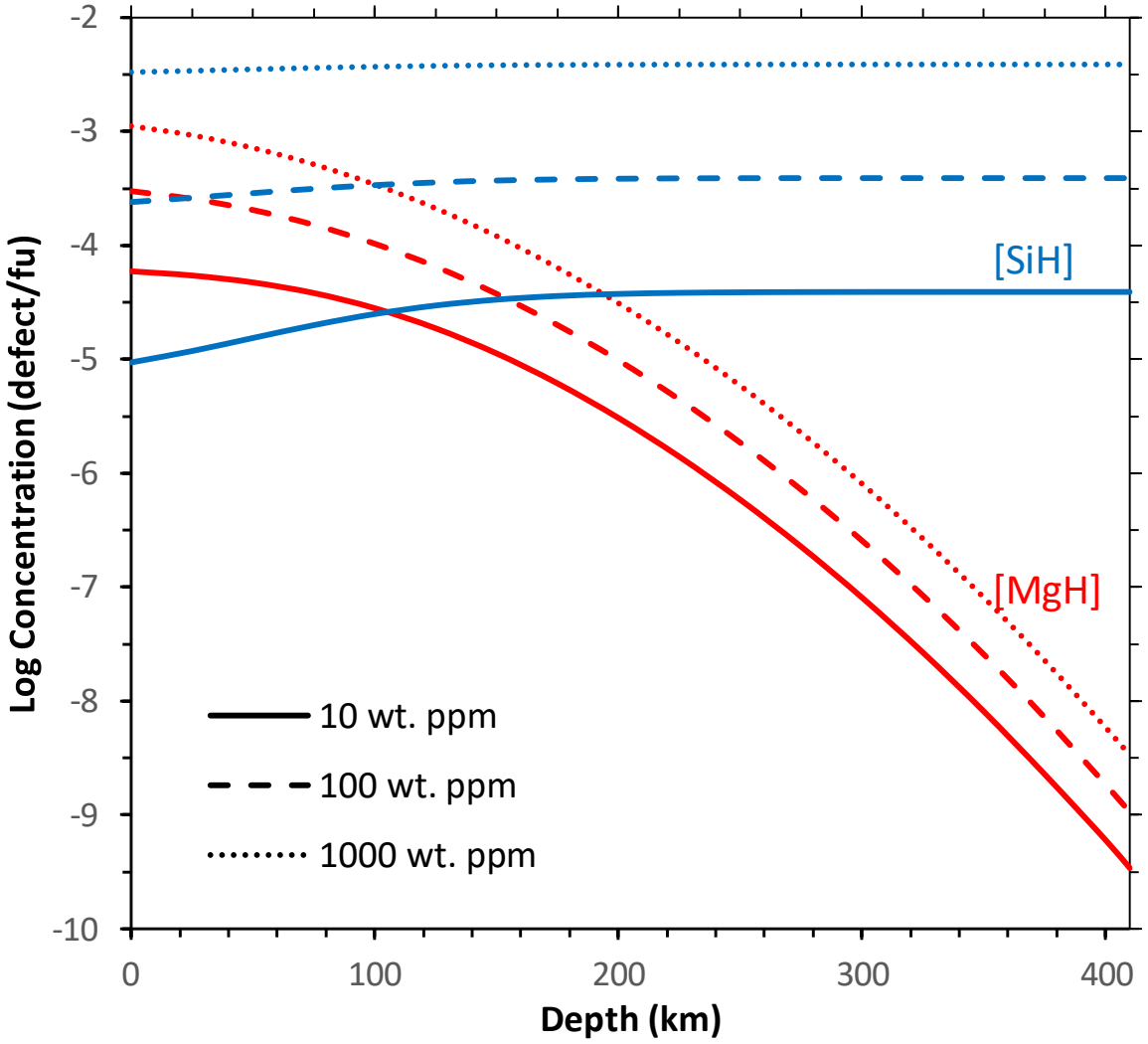

Figure S4: Plot of the distribution of the three major products in pure forsteritealong a geotherm with three different water concentrations (10 wt. ppm=solid lines, 100=dashed lines, 1000=dotted lines).

		Energy (eV)		
Arrangement	Degeneracy	0 GPa (corrected	5	10
O1i O1i	1	0.501	0.503	0.489
O1i O2i	4	0.348	0.002	0.002
O1i O3i	4	0.536	0.561	0.575
O2i O2i	1	0.000	0.000	0.000
O2i O3i	4	0.544	0.525	0.503
O3i O3i	1	0.154	0.161	0.162
O1i O1o	2	1.265	1.370	1.456
O1o O1o	1	2.108	2.300	2.470
O1o O2i	4	1.174	1.269	1.352
O1i O2o	4	1.417	1.085	1.168
O1o O2o	4	2.374	2.585	2.835
O1o O3i	4	1.140	1.242	1.334
O1i O3o	4	0.944	1.048	1.138
O1o O3o	4	1.740	1.930	2.099
O2i O2o	2	0.982	1.085	1.170
O2o O2o	1	2.058	2.265	2.405
O2o O3i	4	1.480	1.586	1.612
O2i O3o	4	1.005	1.094	1.171
O2o O3o	4	2.297	2.515	2.635
O3i O3o	2	0.663	0.745	0.818
O3o O3o	1	1.276	1.435	1.582

Table S1**:** Relative enthalpy of different arrangements of hydrogen in $(2H)^{X}_{Mg}$ as a function of pressure. Each arrangement is defined by the type of oxygen the hydrogen is bound to (O1, O2, O3) and whether it points inside (i) or outside (o) the vacancy with the lowest enthalpy possible for that arrangement listed in every case. Arrangements with hydrogen pointing outside the vacancy are much higher in energy than those where all hydrogen point inside the vacancy. These values are for $(2H)^{X}_{Mg}$ at the M1 site, values at the M2 site are similar but all enthalpies at 0.51/0.59/0.59 eV higher at 0/5/10 GPa (corrected) respectively as $(2H)^{X}_{Mg}$ is favoured at the M1. 0.51/0.59/0.59 eV is used for the site preference enthalpy of $(2H)^{X}_{Mg}$**.**

		Energy (eV)		
Arrangement	Degeneracy	0 GPa (corrected)	5	10
O1i O2i O3i O3i	1	0.494	0.606	0.554
O1o O2i O3i O3i	1	0.334	0.363	0.350
O1i O2o O3i O3i	1	0.000	0.000	0.000
O1i O2iO3o O3i	2	0.036	0.061	0.049
O1o O2o O3i O3i	1	0.350	0.412	0.385
O1o O2i O3o O3i	2	0.434	0.480	0.459
O1i O2o O3o O3i	2	0.136	0.213	0.175
O1i O2i O3o O3o	1	0.285	0.384	0.338
O1o O2o O3o O3i	2	2.200	0.465	0.269
O1i O2o O3o O3o	1	0.465	0.659	0.565
O1o O2i O3o O3o	1	1.914	2.227	2.076
O1o O2o O3o O3o	1	2.469	2.913	2.699

Table S2**:** Relative enthalpy of different arrangements of hydrogen in $(4H)_{Si}^{X}$ as a function of pressure. Each arrangement is defined by the type of oxygen the hydrogen is bound to (O1, O2, O3) and whether it points inside (i) or outside (o) the vacancy with the lowest enthalpy possible for that arrangement listed in every case. The most stable arrangement has one hydrogen pointing outside the vacancy as also found by Qin et al. (2018)**.**

		0 GPa (corrected)						5 GPa						10 GPa				
Arrangement	Degeneracy	M1 A	M1 B	M2 A	M2 B	M2 C	M2 D	M1 A	M1 B	M2 A	M2 B	M2 C	M2 D	M1 A	M1 B	M2 A	M2 B	M2
O3i O3i	**1**	1.759	0.002	1.068	2.347	1.502	0.863	1.810	0.001	1.020	2.243	1.506	0.796	1.850	0.001	0.968	2.140	1.5
O3i O2i	**2**	1.960	1.228	0.995	1.038	1.688	1.085	2.009	0.000	0.923	0.253	1.683	1.041	2.046	0.003	0.857	0.201	1.6
O3i O1i	**2**	1.759	1.114	1.068	1.089	1.500	1.087	1.808	1.095	1.019	1.017	1.505	1.041	1.849	1.067	0.968	0.949	1.5
O2i O1i	**1**	1.961	1.236	1.229	0.316	3.252	3.291	2.009	1.239	1.191	0.264	3.265	3.292	2.046	1.239	1.145	0.216	3.2
O3i O3o	**2**	2.136	0.262	3.677	1.457	1.927	1.547	2.230	0.314	3.753	1.458	1.979	1.539	2.310	0.366	3.813	1.452	2.0
O3o O3o	**1**	2.756	2.641	4.694	4.753	2.584	2.591	2.915	2.799	4.862	4.872	2.706	2.686	3.060	2.942	5.006	4.977	2.8
O3i O2o	**2**	2.181	1.587	1.462	0.431	1.947	3.772	2.258	1.609	1.466	0.412	1.986	3.791	2.327	1.625	1.461	0.400	2.0
O3o O2i	**2**	2.249	0.261	3.783	1.813	2.041	1.454	2.351	0.314	3.855	1.772	2.091	1.480	2.437	0.364	3.905	1.453	2.1
O3o O2o	**2**	2.748	2.659	4.673	2.723	2.543	4.759	2.915	2.805	4.852	2.820	2.666	4.880	3.065	2.938	5.001	2.901	2.7
O3i O1o	**2**	6.759	5.002	6.068	5.316	5.665	5.863	6.810	5.001	6.020	5.264	5.854	5.796	6.850	5.001	5.968	5.216	6.0
O3o O1i	**2**	2.134	0.261	3.572	1.459	1.925	1.455	2.230	0.314	3.685	1.458	1.977	1.480	2.310	0.365	3.771	1.454	2.0
O3o O2o	**2**	2.133	0.261	3.572	1.457	6.239	3.920	2.229	0.313	3.687	1.458	6.503	4.123	2.310	0.364	3.780	1.451	6.7
O2o O1i	**1**	1.924	0.000	3.393	2.111	5.768	5.513	1.965	0.002	3.511	2.164	5.930	1.041	1.994	0.000	1.142	2.220	6.0
O2i O1o	**1**	2.249	1.432	1.466	0.431	3.389	3.736	2.340	1.472	1.466	0.412	1.990	3.808	2.416	1.503	1.463	0.400	2.0
O2o O1o	**1**	2.181	1.430	1.464	2.578	6.240	6.291	2.257	1.473	1.464	2.694	6.469	6.520	2.325	1.500	6.668	2.804	6.6

Table S3 Relative enthalpy of different arrangements of hydrogen in $\{Ti_{Mg}^{\cdot\cdot}(2H)_{Si}^{\prime\prime}\}$ as a function of pressure. Each arrangement is defined by the type of oxygen the hydrogen is bound to (O1, O2, O3) and whether it points inside (i) or outside (o) the vacancy with the lowest enthalpy possible for that arrangement listed in every case. There are 6 Ti sites relative to the $(2H)_{Mg}^{X}$ (see (Walker et al., 2007)), 2 in an M1 site which are each 2 fold degenerate and 4 in an M2 site which are each 1 fold degenerate.

		Energy (eV)		
Arrangement	Degeneracy	0 GPa (corrected	5	10
O1i	2	0.263	0.267	0.264
O1o	2	1.149	1.255	1.350
O2i	2	0.000	0.000	0.000
O2o	2	1.132	1.240	1.337
O3i	2	0.063	0.064	0.063
O3o	2	0.723	0.809	0.890

Table S4**:** Relative enthalpy of different arrangements of hydrogen in $(1H)'_{Mg}$ as a function of pressure. Each arrangement is defined by the type of oxygen the hydrogen is bound to (O1, O2, O3) and whether it points inside (i) or outside (o) the vacancy with the lowest enthalpy possible for that arrangement listed in every case. Arrangements with hydrogen pointing outside the vacancy are much higher in energy than those where all hydrogen point inside the vacancy.

		Energy (eV)		
Arrangement	Degeneracy	0 GPa (corrected)	5	10
O1i O3i O3i	1	0.285	0.320	0.298
O2i O3i O3i	1	0.000	0.001	0.001
O1i O2i O3i	2	0.405	0.000	0.000
O1i O3o O3i	2	0.545	0.656	0.609
O1o O3i O3i	1	0.283	1.003	0.314
O1o O3o O3i	2	0.544	0.663	0.611
O1i O3o O3o	1	0.921	1.141	1.040
O1o O3o O3o	1	3.271	3.853	3.577
O2i O3o O3i	2	0.492	0.568	0.534
O2o O3i O3i	1	0.332	0.397	0.367
O2o O3o O3i	2	1.041	1.224	1.137
O2i O3o O3o	1	1.170	1.143	1.258
O2o O3o O3o	1	2.154	2.582	2.378
O1i O2i O3o	1	0.659	0.800	0.739
O1i O2o O3i	1	0.522	0.609	0.573
O1o O2i O3i	1	0.404	1.087	1.036
O1i O2o O3o	1	0.902	1.137	1.025
O1o O2i O3o	1	2.785	3.249	3.033
O1o O2o O3i	1	0.520	0.886	0.721
O1o O2o O3o	1	0.898	1.171	1.044

Table S5**:** Relative enthalpy of different arrangements of hydrogen in $(3H)'_{Si}$ as a function of pressure. Each arrangement is defined by the type of oxygen the hydrogen is bound to (O1, O2, O3) and whether it points inside (i) or outside (o) the vacancy with the lowest enthalpy possible for that arrangement listed in every case.

	0 GPa			5 GPa			10 GPa		
	1000 K	1500 K	2000 K	1000 K	1500 K	2000 K	1000 K	1500 K	2000 K
R9	-2.179	-2.814	-3.198	-2.166	-2.934	-3.480	-2.124	-2.994	-3.678
R10	-0.959	-1.296	-1.680	-0.949	-1.311	-1.747	-0.951	-1.311	-1.776
R12	10.268	11.156	11.934	10.531	11.612	12.559	10.915	12.184	13.291
R13	25.757	32.592	40.442	26.195	32.219	39.363	27.542	32.586	38.873
R14	5.622	5.226	4.855	5.335	4.742	4.202	5.161	4.354	3.625
R15	7.092	8.211	9.304	6.988	8.275	9.528	6.868	8.272	9.668
R16	9.077	9.261	9.491	9.144	9.478	9.852	9.355	9.817	10.313
R17	20.114	21.857	23.571	19.619	21.462	23.365	19.206	21.056	23.068
R18	19.748	26.901	35.046	20.472	27.012	34.620	21.994	27.768	34.707
R19	9.077	9.261	9.491	9.144	9.478	9.852	9.355	9.817	10.313
R20	18.224	18.883	19.160	17.096	17.793	18.425	16.271	16.889	17.587
R21	36.437	39.543	43.304	37.252	41.554	45.818	39.306	43.776	48.399

Table S6: Reaction energies (in eV/f.u) for minor reactions as a function of pressure and temperature.

			$[H_2O]_{bulk}$ wt. ppm							
Temp	Pressure	$[Al_2O_3]$ wt. ppm	1	5	10	25	50	100	250	500
2000 K	5	10	1.349	1.005	1.017	1.074	1.201	1.509	2.665	5.213
		25	1.240	1.002	1.007	1.030	1.082	1.205	1.628	2.410
		50	1.161	1.001	1.004	1.016	1.042	1.105	1.317	1.684
		100	1.101	1.001	1.002	1.008	1.022	1.055	1.165	1.351
		250	1.052	1.000	1.001	1.004	1.010	1.024	1.073	1.155
		500	1.031	1.000	1.000	1.002	1.006	1.014	1.042	1.088
	10	10	1.001	1.013	1.032	1.094	1.194	1.380	1.892	2.702
		25	1.000	1.006	1.014	1.041	1.085	1.166	1.379	1.694
		50	1.000	1.003	1.008	1.023	1.048	1.093	1.212	1.384
		100	1.000	1.002	1.005	1.014	1.028	1.055	1.125	1.225
		250	1.000	1.001	1.002	1.007	1.015	1.029	1.066	1.119
		500	1.000	1.001	1.002	1.005	1.010	1.019	1.042	1.077
	15	10	1.000	1.000	1.000	1.000	1.000	1.001	1.002	1.005
		25	1.000	1.000	1.000	1.000	1.000	1.001	1.001	1.003
		50	1.000	1.000	1.000	1.000	1.000	1.000	1.001	1.002
		100	1.000	1.000	1.000	1.000	1.000	1.000	1.001	1.001
		250	1.000	1.000	1.000	1.000	1.000	1.000	1.000	1.001
		500	1.000	1.000	1.000	1.000	1.000	1.000	1.000	1.000
1500 K	5	10	1.003	1.024	1.054	1.149	1.300	1.581	2.373	3.711
		25	1.001	1.010	1.023	1.064	1.127	1.243	1.550	2.010
		50	1.001	1.005	1.013	1.035	1.069	1.133	1.297	1.534
		100	1.000	1.003	1.007	1.020	1.040	1.076	1.169	1.302
		250	1.000	1.002	1.004	1.010	1.020	1.039	1.086	1.153
		500	1.000	1.001	1.002	1.006	1.013	1.024	1.054	1.097
	10	10	1.001	1.004	1.007	1.014	1.023	1.040	1.079	1.134
		25	1.001	1.002	1.004	1.007	1.012	1.021	1.042	1.071
		50	1.000	1.001	1.002	1.005	1.008	1.014	1.027	1.046
		100	1.000	1.001	1.002	1.003	1.005	1.009	1.018	1.030
		250	1.000	1.001	1.001	1.002	1.003	1.005	1.011	1.018
		500	1.000	1.000	1.001	1.001	1.002	1.004	1.007	1.012
	15	10	1.000	1.000	1.000	1.000	1.000	1.000	1.000	1.000
		25	1.000	1.000	1.000	1.000	1.000	1.000	1.000	1.000
		50	1.000	1.000	1.000	1.000	1.000	1.000	1.000	1.000
		100	1.000	1.000	1.000	1.000	1.000	1.000	1.000	1.000
		250	1.000	1.000	1.000	1.000	1.000	1.000	1.000	1.000
		500	1.000	1.000	1.000	1.000	1.000	1.000	1.000	1.000
1000 K	5	10	1.000	1.000	1.001	1.002	1.005	1.008	1.013	1.016
		25	1.000	1.000	1.001	1.001	1.003	1.005	1.008	1.011

		50	1.000	1.000	1.001	1.001	1.002	1.003	1.006	1.191
		100	1.002	1.006	1.010	1.020	1.034	1.057	1.113	1.104
		250	1.001	1.003	1.005	1.011	1.018	1.031	1.061	1.045
		500	1.001	1.002	1.004	1.007	1.012	1.020	1.027	1.027
	10	10	1.000	1.000	1.001	1.002	1.003	1.004	1.008	1.014
		25	1.000	1.000	1.000	1.001	1.002	1.003	1.005	1.009
		50	1.000	1.000	1.000	1.001	1.001	1.002	1.004	1.006
		100	1.000	1.000	1.000	1.001	1.001	1.001	1.003	1.004
		250	1.000	1.000	1.000	1.000	1.000	1.001	1.002	1.003
		500	1.000	1.000	1.000	1.000	1.000	1.001	1.001	1.002
	15	10	1.000	1.000	1.000	1.000	1.000	1.000	1.000	1.000
		25	1.000	1.000	1.000	1.000	1.000	1.000	1.000	1.000
		50	1.000	1.000	1.000	1.000	1.000	1.000	1.000	1.000
		100	1.000	1.000	1.000	1.000	1.000	1.000	1.000	1.000
		250	1.000	1.000	1.000	1.000	1.000	1.000	1.000	1.000
		500	1.000	1.000	1.000	1.000	1.000	1.000	1.000	1.000

Table S7: ($Al_{Mg}^{\cdot}/Al_{Si}^{\prime}$) as a function of Al content, pressure, temperature and water content. For most conditions these are identical ($Al_{Mg}^{\cdot} = Al_{Si}^{\prime}$) which is the base state but at high temperatures, low pressures and low Aluminium large amounts of water changes this ratio significantly and in near linear fashion. In these conditions water concentration has a near linear effect on the ratio and thus measuring the ratio can tell you the water content.

			$[H_2O]_{bulk}$ wt. ppm							
Temp	Pressure	$[TiO_2]$ wt. ppm	1	5	10	25	50	100	250	500
2000 K	5	10	1.882	1.189	0.894	0.514	0.240	-0.018	-0.328	-0.541
		25	1.901	1.206	0.910	0.527	0.250	-0.012	-0.325	-0.539
		50	1.930	1.234	0.936	0.548	0.265	-0.001	-0.320	-0.536
		100	1.983	1.285	0.984	0.589	0.297	0.020	-0.310	-0.531
		250	2.113	1.411	1.106	0.698	0.388	0.084	-0.279	-0.515
		500	2.269	1.566	1.259	0.846	0.523	0.192	-0.223	-0.486
	10	10	1.577	0.935	0.684	0.384	0.179	-0.012	-0.248	-0.418
		25	1.612	0.961	0.704	0.397	0.186	-0.007	-0.245	-0.416
		50	1.665	1.002	0.737	0.417	0.199	0.000	-0.242	-0.414
		100	1.757	1.078	0.799	0.458	0.226	0.016	-0.234	-0.410
		250	1.956	1.259	0.961	0.578	0.308	0.065	-0.212	-0.398
		500	2.165	1.462	1.157	0.749	0.443	0.154	-0.171	-0.377
	15	10	2.625	2.271	2.119	1.919	1.768	1.616	1.416	1.264
		25	2.628	2.272	2.120	1.919	1.768	1.617	1.416	1.264
		50	2.631	2.273	2.121	1.920	1.768	1.617	1.417	1.264
		100	2.637	2.276	2.122	1.921	1.769	1.617	1.417	1.264
		250	2.654	2.283	2.128	1.924	1.771	1.619	1.418	1.265
		500	2.683	2.296	2.137	1.929	1.775	1.621	1.419	1.266
1500 K	5	10	0.987	0.325	0.068	-0.236	-0.440	-0.628	-0.861	-1.029
		25	1.107	0.408	0.124	-0.209	-0.426	-0.621	-0.858	-1.027
		50	1.259	0.534	0.219	-0.160	-0.401	-0.609	-0.853	-1.025
		100	1.466	0.732	0.396	-0.054	-0.346	-0.582	-0.843	-1.020
		250	1.798	1.076	0.746	0.263	-0.142	-0.487	-0.809	-1.004
		500	2.076	1.364	1.045	0.594	0.196	-0.271	-0.744	-0.975
	10	10	1.240	0.851	0.691	0.483	0.329	0.280	0.025	-0.151
		25	1.287	0.870	0.704	0.491	0.333	-0.028	-0.182	-0.336
		50	1.362	0.903	0.726	0.504	0.177	-0.027	-0.181	-0.335
		100	1.498	0.969	0.771	0.529	0.182	-0.024	-0.179	-0.335
		250	1.790	1.151	0.903	0.609	0.192	-0.019	-0.176	-0.333
		500	2.066	1.380	1.095	0.741	0.224	-0.003	-0.167	-0.328
	15	10	3.389	3.039	2.891	2.691	2.542	2.390	2.191	2.039
		25	3.393	3.043	2.893	2.694	2.543	2.391	2.192	2.040
		50	3.394	3.043	2.894	2.694	2.543	2.392	2.192	2.040
		100	3.395	3.044	2.894	2.694	2.543	2.392	2.192	2.040
		250	3.398	3.045	2.895	2.695	2.543	2.392	2.192	2.039

		500	3.403	3.049	2.896	2.695	2.543	2.392	2.192	2.039
1000 K	5	10	1.882	1.189	0.894	0.514	0.240	-0.018	-0.328	-0.541
		25	1.901	1.206	0.910	0.527	0.250	-0.012	-0.325	-0.539
		50	1.930	1.234	0.936	0.548	0.265	-0.001	-0.320	-0.536
		100	1.983	1.285	0.984	0.589	0.297	0.020	-0.310	-0.531
		250	2.113	1.411	1.106	0.698	0.388	0.084	-0.279	-0.515
		500	2.269	1.566	1.259	0.846	0.523	0.192	-0.223	-0.486
	10	10	1.577	0.935	0.684	0.384	0.179	-0.012	-0.248	-0.418
		25	1.612	0.961	0.704	0.397	0.186	-0.007	-0.245	-0.416
		50	1.665	1.002	0.737	0.417	0.199	0.000	-0.242	-0.414
		100	1.757	1.078	0.799	0.458	0.226	0.016	-0.234	-0.410
		250	1.956	1.259	0.961	0.578	0.308	0.065	-0.212	-0.398
		500	2.165	1.462	1.157	0.749	0.443	0.154	-0.171	-0.377
	15	10	2.625	2.271	2.119	1.919	1.768	1.616	1.416	1.264
		25	2.628	2.272	2.120	1.919	1.768	1.617	1.416	1.264
		50	2.631	2.273	2.121	1.920	1.768	1.617	1.417	1.264
		100	2.637	2.276	2.122	1.921	1.769	1.617	1.417	1.264
		250	2.654	2.283	2.128	1.924	1.771	1.619	1.418	1.265
		500	2.683	2.296	2.137	1.929	1.775	1.621	1.419	1.266

Table S8: Log of $(Ti_{Si}^{X}/Ti_{Mg}^{\cdot\cdot})$ as a function of Ti content, pressure, temperature and water content. Adding water decreases this ratio by making more $\{Ti_{Mg}^{\cdot\cdot}(2H)_{Si}^{\prime\prime}\}$, adding more Ti or increasing the temperature increases this ratio, changing the pressure has varied effect depending upon temperature. The effect of water on the value is nearly linear within a set P, T and Ti concentration for all conditions and thus measuring this ratio is a good measurement of water concentration.

	Static			1500 K			Key Concentration (0 GPa 1500 K)	Conclusion
	0 GPa	5	10	0	5	10		
$Al_{Mg}^{\bullet}+(1H)_{Mg}'$	-0.68	-0.82	-0.83	not examined	not examined	not examined	7200.548	Unbound
$Al_{Si}'+H_{int}^{\cdot}$	-2.26	-2.48	-2.55	-1.68	-2.00	-2.11	1127.549	Unbound
$Al_{Mg}^{\bullet}+(3H)_{Si}'$	-0.93	-0.95	-0.95	not examined	not examined	not examined	3020.346	Unbound
$Ti_{Mg}^{\cdot\cdot} + (2H)_{Si}''$	-5.00	-5.69	-5.74	not examined	not examined	not examined	<0.01	Bound

Table S9: Binding energy of some defect pairs. $Al_{Mg}^{\cdot} + Al_{Si}'$ is R10 (Table S6) and $2 * Al_{Mg}^{\cdot}+V_{Mg}''$ is R9 (Table S6). In each case we present the energy and then a key concentration which is the concentration at which the preference goes from unbound to bound pairs in a simplified system in which only these defects exist and they behave perfectly.

Depth (km)	Temp (K)	Pressure (GPa)	Ti+Al concentration (oxide wt. ppm)
0	1575.00	0.00	488.27
25	1586.28	0.83	370.43
50	1597.56	1.67	282.35
75	1608.84	2.50	216.21
100	1620.12	3.34	166.30
125	1631.40	4.17	128.47
150	1642.68	5.01	99.67
175	1653.96	5.84	77.65
200	1665.24	6.68	60.74
225	1676.52	7.51	47.70
250	1687.80	8.35	37.60
275	1699.09	9.18	29.75
300	1710.37	10.01	23.63
325	1721.65	10.85	18.83
350	1732.93	11.68	15.07
375	1744.21	12.52	12.09
400	1755.49	13.35	9.74
410	1760.00	13.69	8.94

Table S10: Details of our geotherm and the concentration of products along it. These points were achieved by extrapolation from Ono (2008) whereas those of Al concentration were from solving equation 13 in De Hoog et al. (2010) adjusted for Al_2O_3 weight. TiO_2 was set to the same as Al_2O_3 weight**.** All runs along a geotherm used these points, for some runs additional points were necessary for smoothing and these were determined by interpolating between the 3 nearest points.

		Energy (eV)		
Arrangement	Degeneracy	0 GPa (corrected)	5	10
M1a-Si	1	0.315	0.323	0.329
M1b-Si	1	0.001	0.000	0.000
M1c-Si	1	0.000	0.000	0.000
M1d-Si	1	0.315	0.323	0.329
M2a-Si	1	0.128	0.063	0.006
M2b-Si	1	0.356	0.305	0.259
M2c-Si	1	0.340	0.294	0.255
M2d-Si	1	0.331	0.284	0.242

Table S11**:** Relative enthalpy of different arrangements of $\{Al_{Mg}^{\cdot} Al_{Si}^{\prime}\}$. In each case the $Al_{Mg}^{\cdot}$ was on a nearest neighbour or a next nearest.

Arrangement	Degeneracy	0 GPa (corrected)	Arrangement	Degeneracy	0 GPa (corrected)
M1-M1-M1	1	0.941	M2-M2-M2	1	2.249
M1-M1-M1	1	0.085	M2-M2-M2	4	2.181
M1-M1-M1	4	1.356	M2-M2-M2	4	1.946
M1-M1-M1	4	1.008	M2-M2-M2	4	1.966
M1-M1-M1	4	0.736	M2-M2-M2	4	1.931
M1-M1-M1	4	0.614	M2-M2-M2	4	2.276
M1-M1-M1	4	0.634	M2-M2-M2	4	1.841
M1-M1-M1	4	1.128	M2-M2-M2	2	1.758
M1-M1-M1	2	1.057	M1-M2-M1	4	1.799
M2-M1-M2	2	0.669	M1-M2-M1	2	1.789
M2-M1-M2	4	0.614	M1-M2-M1	1	1.623
M2-M1-M2	2	0.742	M1-M2-M1	4	1.503
M2-M1-M2	2	0.590	M1-M2-M1	4	1.461
M2-M1-M2	4	0.356	M2-M2-M1	4	2.008
M2-M1-M2	1	0.000	M2-M2-M1	4	2.210
M2-M1-M1	4	0.969	M2-M2-M1	4	1.895
M2-M1-M1	4	0.757	M2-M2-M1	4	2.268
M2-M1-M1	4	0.562	M2-M2-M1	4	2.026
M2-M1-M1	8	0.541	M2-M2-M1	2	1.871
M2-M1-M1	2	0.506	M2-M2-M1	2	1.754
M2-M1-M1	2	0.081	M2-M2-M1	4	1.723
M2-M1-M1	8	0.949	M2-M2-M1	4	1.778
M2-M1-M1	8	0.820	M2-M2-M1	4	1.870
M2-M1-M1	4	0.697	M2-M2-M1	4	2.029
M2-M1-M1	4	0.540	M2-M2-M1	4	1.625
M2-M2-M2	1	2.292	M2-M2-M1	4	1.793

Table S12**:** Relative enthalpy of different arrangements of $\{Al_{Mg}^{\cdot} - V_{Mg}^{''} - Al_{Mg}^{\cdot}\}$. Only enthalpy at 0 GPa was considered but considering the high relative enthalpy of nearly all arrangements except for 3 it is unlikely pressure or temperature has an effect on the configurational entropy. In each case a $Al_{Mg}^{\cdot}$ was placed in an M1 or an M2 site, $V_{Mg}^{''}$ was placed in a next-nearest site and then $Al_{Mg}^{\cdot}$ in a next nearest site to the $V_{Mg}^{''}$. The most stable arrangements have all three sites in a single line.

		0 GPa	5	10
$(2H)^{X}_{Mg}$	M1	0.000	0.000	0.000
	M2	0.626	0.687	0.729
$(1H)'_{Mg}$	M1	0.000	0.000	0.000
	M2	0.848	0.909	0.951
$H_{Int}^{\cdot}$	O1	0.000	0.000	0.000
	O2	0.326	0.301	0.275
	O3	0.326	0.299	0.275
V''_{Mg}	M1	0.000	0.000	0.000
	M2	1.117	1.199	1.250
$Mg_I^{\bullet\bullet}$	M1	0.000	0.000	0.000
	I2 Static	-0.004	-0.155	-0.237
	I2 1000 K	0.315	0.209	0.192
	I2 2000 K	0.468	0.372	0.378
	I2 1000 K	0.623	0.524	0.543
$Al_{Mg}^{\bullet}$	M1	0.000	0.000	0.000
	M2	0.012	-0.055	-0.107
$V_O^{\bullet\bullet}$	O1	2.269	2.327	2.367
	O2	0.806	0.731	0.655
	O3	0.000	0.000	0.000
O_I''	I1	1.203	1.180	1.156
	I2	0.015	0.016	0.016
	T1	1.487	1.542	1.609
	T2	0.000	0.000	0.000
	T3	0.015	0.017	0.015
	T4	0.741	0.889	1.027
	T5	0.017	0.018	0.016
$Si_I^{\bullet\bullet\bullet\bullet}$	I1	4.130	4.122	4.114
	I2	1.927	1.821	1.978
	T1	0.279	0.000	0.000
	T2	1.660	1.519	1.641
	T3	0.000	0.149	0.530
	T4	0.000	0.150	1.654
	T5	3.010	3.246	3.482

Table S13 Relative Enthalpy of different defects in different crystallographic sites- for sites containing hydrogen this is in their most stable arrangement. For $Mg_I^{\bullet\bullet}$ temperature variation is also shown to relative to the M1 site which is always set to 0. For definition of the O and Si interstitial sites see Muir et al. (2020).

DE HOOG, J. C. M., GALL, L. & CORNELL, D. H. 2010. Trace-element geochemistry of mantle olivine and application to mantle petrogenesis and geothermobarometry. *Chemical Geology,* 270**,** 196-215.

MUIR, J., ZHANG, F. & WALKER, A. M. Submitted. The Controls of Pressure and Water on Highly Anisotropic Mg Diffusion in Forsterite**.,** Preprint available at https://doi.org/10.31223/osf.io/ck3af.

MUIR, J. M. R., JOLLANDS, M., ZHANG, F. W. & WALKER, A. M. 2020. Explaining the dependence of M-site diffusion in forsterite on silica activity: a density functional theory approach. *Physics and Chemistry of Minerals,* 47.

ONO, S. 2008. Experimental constraints on the temperature profile in the lower mantle. *Physics of the Earth and Planetary Interiors,* 170**,** 267-273.

QIN, T., WENTZCOVITCH, R. M., UMEMOTO, K., HIRSCHMANN, M. M. & KOHLSTEDT, D. L. 2018. Ab initio study of water speciation in forsterite: Importance of the entropic effect. *American Mineralogist,* 103**,** 692-699.

WALKER, A. M., HERMANN, J., BERRY, A. J. & O'NEILL, H. S. C. 2007. Three water sites in upper mantle olivine and the role of titanium in the water weakening mechanism. *Journal of Geophysical Research-Solid Earth,* 112.